Direct Numerical Simulation Studies on the Dynamics of Dispersed Particles in a Compressible Fluid

Rei Tatsumi

2013

Contents

Chapter 1

General introduction

1.1   Introductory remarks

A dispersion is a system in which small particles are dispersed in a continuous medium. The size of particles is between approximately 1 nm (10^{-9} m) and 1 μm (10^{-6} m). There are various dispersions in industrial processes and products as powder particles in a gas or colloidal particles in a solution. In such dispersions, each dispersed particle exerts forces on the others not only through thermodynamic potential interactions, such as electrostatic or London dispersion forces, but also through dynamical interactions referred to as hydrodynamic interactions, which correspond to the momentum exchange among particles through the ambient fluid.[1] In dynamic processes such as aggregation, sedimentation, and electrophoresis, the hydrodynamic interactions characterize the particle motion and dynamical properties of the dispersion. Therefore, many studies for the quantitative estimation of hydrodynamic interactions have been conducted.[1–3]

The spatiotemporal scales of the dynamics of dispersed particles are much larger than those of molecules making up the host fluid; therefore, in the investigation of the hydrodynamic interactions, the host fluid can be treated as a continuum in disregard of detailed molecular information. In this coarse-graining model, the dynamics of a dispersion is formulated as a problem of fluid dynamics with boundary conditions imposed on the surface of particles. In general, however, the analysis of problems in this formulation is mathematically difficult. Therefore, in the first place, the formulation is reconstructed by assuming a quasi-steady flow (Stokes flow),[2,3] in which the motion of fluid is assumed to instantaneously follow that of particles. In this assumption, some approximate analytical solutions for a particle pair are derived in simple forms; for example, the Rotne-Pragar-Yamakawa (RPY) mobility tensor is well known.[4,5] In early numerical methods to simulate the dynamics of dispersions, the hydrodynamic interactions are incorporated by the superposition of the pair mobility tensors such as the RPY tensor.[6,7] However, such methods cannot describe the details of the propagation process of hydrodynamic interactions.

Later, various numerical solutions and modelizations have been devised to solve the hydrodynamic equations,[8–12] thereby considering the propagation process of hydrodynamic interactions.

However, the host fluid is usually assumed to be incompressible, i.e., the change in the fluid density is ignored. The fluid incompressibility corresponds to the infinite speed of sound. In a fluid, the momentum, namely the hydrodynamic interaction, is transferred by two mechanisms: sound propagation and viscous diffusion;[13] therefore, in an incompressible fluid, only the viscous diffusion is explicitly considered in the propagation process of hydrodynamic interactions. The assumption of the fluid incompressibility is based on the fact that the time scale of sound propagation is much shorter than that of viscous diffusion in many cases. However, the fluid compressibility must be considered when we are interested in the properties of short-time scale such as acoustic properties and investigate the dynamics of dispersions with highly viscous fluid. Because there have been little interest in such situations in addition to the requirement of special numerical analytical approaches to treat compressible fluids, the fluid compressibility effects on the dynamics of dispersions are not well understood. In this dissertation, we develop the direct numerical simulation method for dispersions with compressible fluids and reveal the fluid compressibility effects on the propagating hydrodynamic interactions.

1.2   Theoretical formulation

In the coarse-graining model of a dispersion, the fluid motion is described by the hydrodynamic equations, and the motion of dispersed particles are described by Newton's and Euler's equations of motion. These equations are coupled through the conservation of momentum and energy between the fluid and the particles. In other words, the surface of the particles gives the boundary conditions for the hydrodynamic equations, and at the same time, the fluid exerts the hydrodynamic force on the particles and works as the heat medium for them.

The hydrodynamic equations consist of three conservation laws concerning mass, momentum, and energy, which are given as

$$\frac{\partial \rho}{\partial t} + \boldsymbol{\nabla} \cdot (\rho \boldsymbol{v}) = 0, \tag{1.1}$$

$$\frac{\partial \rho \boldsymbol{v}}{\partial t} + \boldsymbol{\nabla} \cdot (\rho \boldsymbol{v} \boldsymbol{v}) = \boldsymbol{\nabla} \cdot \boldsymbol{\sigma}, \tag{1.2}$$

$$\frac{\partial \rho e}{\partial t} + \boldsymbol{\nabla} \cdot (\rho e \boldsymbol{v}) = -\boldsymbol{\nabla} \cdot \boldsymbol{q} + \boldsymbol{\sigma} : \boldsymbol{\nabla} \boldsymbol{v}, \tag{1.3}$$

where ρ is the mass density, $\boldsymbol{v}$ is the velocity field, e is the energy density, $\boldsymbol{\sigma}$ is the stress tensor, and $\boldsymbol{q}$ is the heat current. The stress tensor and the heat current are respectively related to the gradients

2

of velocity field and temperature through the constitutive equations. In the linear formulation, the constitutive equation of stress tensor is given by

$$\boldsymbol{\sigma} = -p\boldsymbol{I} + \eta[\boldsymbol{\nabla v} + (\boldsymbol{\nabla v})^T] + \left(\eta_v - \frac{2}{3}\eta\right)(\boldsymbol{\nabla} \cdot \boldsymbol{v})\boldsymbol{I}, \tag{1.4}$$

where p is the pressure, η is the shear viscosity, and η_v is the bulk viscosity. The fluid satisfying the relation Eq. (1.4) is called a Newtonian fluid. The heat current is also given by the Fourier's law as

$$\boldsymbol{q} = -k\boldsymbol{\nabla}T, \tag{1.5}$$

where T is the temperature, and k is the thermal conductivity. Additionally, the thermodynamic quantities are connected by the equations of state $e = e(\rho, T)$ and $p = p(\rho, T)$. Equations (1.1)-(1.5) with two equations of state are closed for the velocity field $\boldsymbol{v}$ and any two thermodynamic quantities.

The motion of the particles is governed by Newton's and Euler's equations of motion as

$$M_i \frac{\mathrm{d}}{\mathrm{d}t}\boldsymbol{V}_i = \boldsymbol{F}_i^H + \boldsymbol{F}_i^C + \boldsymbol{F}_i^E, \quad \frac{\mathrm{d}}{\mathrm{d}t}\boldsymbol{R}_i = \boldsymbol{V}_i, \tag{1.6}$$

$$\boldsymbol{I}_i \cdot \frac{\mathrm{d}}{\mathrm{d}t}\boldsymbol{\Omega}_i = \boldsymbol{N}_i^H + \boldsymbol{N}_i^E, \tag{1.7}$$

where $\boldsymbol{R}_i$, $\boldsymbol{V}_i$, and $\boldsymbol{\Omega}_i$ are the position, translational velocity, and rotational velocity of the i-th particle, respectively. The particle has a mass M_i and a moment of inertia $\boldsymbol{I}_i$. The hydrodynamic force $\boldsymbol{F}_i^H$ and torque $\boldsymbol{N}_i^H$ are exerted on the particle by the fluid, and the force $\boldsymbol{F}_i^C$ is exerted through direct interactions among the particles. A force $\boldsymbol{F}_i^E$ and torque $\boldsymbol{N}_i^E$ are externally applied. According to the momentum conservation between the fluid and the particle, the hydrodynamic force and torque are given by

$$\boldsymbol{F}_i^H = \int \mathrm{d}\boldsymbol{S}_i \cdot \boldsymbol{\sigma}, \tag{1.8}$$

$$\boldsymbol{N}_i^H = \int (\boldsymbol{r} - \boldsymbol{R}_i) \times (\mathrm{d}\boldsymbol{S}_i \cdot \boldsymbol{\sigma}), \tag{1.9}$$

where the integrations are performed over the surface of the particle. As a result of the energy conservation, the thermal exchange between the fluid and the particle are also considered. Assuming that the temperature distributes uniformly inside the particle, the thermal exchange results in

$$C_i \frac{\mathrm{d}T_i^p}{\mathrm{d}t} = \int \mathrm{d}\boldsymbol{S}_i \cdot \boldsymbol{q}, \tag{1.10}$$

3

Table 1.1: Time scales of physical processes which occur in dispersions.

Viscous diffusion	$\tau_\nu = \dfrac{a^2}{\nu}$
Sound propagation	$\tau_c = \dfrac{a}{c}$
Thermal conduction	$\tau_\alpha = \dfrac{a^2}{\alpha}$
Particle diffusion	$\tau_D = \dfrac{a^2}{D_p} = \dfrac{6\pi\eta a^3}{k_B T}$

where T_i^p and C_i are the temperature and the heat capacity of the i-th particle, respectively. At the same time, the velocity and temperature of the particles impose the boundary conditions on the hydrodynamic equations at the surface of them.

1.3 Time scales

A dispersion is a multi-time scale system in which multiple physical processes occur in different time scales. In the theoretical analysis, the disregard of the physical processes occurring in a time scale largely separated from that of phenomena of interest is justified; correspondingly, the hydrodynamic equations can be simplified.

The time scales of physical processes in a dispersion are summarized in Table 1.1. To estimate these time scales, the particle radius a is selected as the characteristic length of the system. The momentum is transmitted in the fluid according to Eq. (1.2), in which two mechanisms of transmission are included: viscous diffusion and sound propagation. Each of them occurs in different time scales $\tau_\nu = a^2/\nu$ and $\tau_c = a/c$, respectively, where $\nu = \eta/\rho_0$ is the kinematic viscosity, ρ_0 is the mass density in equilibrium, and c is the speed of sound. As described in Eq. (1.3), heat transfer, or thermal conduction occurs to reduce the temperature inhomogeneity. The time scale of the thermal conduction is given by $\tau_\alpha = a^2/\alpha$, where $\alpha = k/(\rho_0 c_p)$ is the thermal diffusivity and c_p is the specific heat capacity in isobaric process. In a dispersion, the diffusion of dispersed particles is also an important physical process. The time scale of the particle diffusion is given by $\tau_D = a^2/D_p$, where D_p is the particle diffusion coefficient. According to the Stokes-Einstein
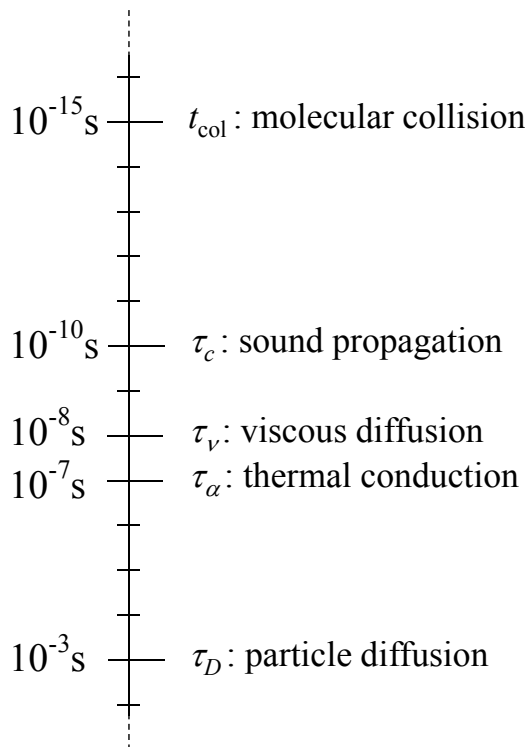
Figure 1.1: The order of time scales of physical processes in a dispersion. A system in which dispersed particles of radius 100 nm are dispersed in a water is considered. The mechanical properties of water at room temperature (around 25 degrees Centigrade) are $\nu = 1.0 \times 10^{-6}$ m/s^2, $c = 1.5 \times 10^3$ m/s, and $\alpha = 1.4 \times 10^{-5}$ m/s^2.

relation, the particle diffusion coefficient is given by

$$D_p = \frac{k_B T}{6\pi\eta a},\tag{1.11}$$

where k_B is the Boltzmann constant. When we consider a dispersion composed by particles of radius $a = 100$ nm and a water, the order of time scales of physical processes in the system is presented in Fig. 1.1. Every physical process accompanied by the motion of fluid and particles occurs in much slower time scale than that of molecular collision; therefore, the coarse-graining model of dispersion is validated. In the same way, the hydrodynamic equations can be simplified by ignoring physical processes which occur in widely different time scale from that of the interesting phenomenon.

To construct the simplified hydrodynamic equations, we rewrite Eqs. (1.1) and (1.2) in Lagrange description with the non-dimensionalization of variables:

$$\mathrm{St}\frac{\delta\rho_1}{\rho_0}\frac{D\tilde{\rho}}{D\tilde{t}} = -\tilde{\rho}\tilde{\boldsymbol{\nabla}}\cdot\tilde{\boldsymbol{v}},\tag{1.12}$$

Table 1.2: Dimensionless numbers which appear in the non-dimensionalized hydrodynamic equations. The time scale of our observation is t_o. The time scale of fluid advection is $\tau_{\mathrm{ad}} = a/V$, where V is the characteristic velocity in the system. The characteristic changes in pressure and temperature are respectively represented by δp_1 and δT_1.

Strouhal number	$\mathrm{St} = \dfrac{a}{Vt_o} = \dfrac{\tau_{\mathrm{ad}}}{t_o}$
Reynolds number	$\mathrm{Re} = \dfrac{aV}{\nu} = \dfrac{\tau_\nu}{\tau_{\mathrm{ad}}}$
Mach number	$\mathrm{Ma} = \dfrac{V}{c} = \dfrac{\tau_c}{\tau_{\mathrm{ad}}}$
Prandtl number	$\mathrm{Pr} = \dfrac{\nu}{\alpha} = \dfrac{\tau_\alpha}{\tau_\nu}$
Euler number	$\mathrm{Eu} = \dfrac{\delta p_1}{\rho_0 V^2}$
Eckert number	$\mathrm{Ec} = \dfrac{V^2}{c_p \delta T_1}$

$$\mathrm{ReSt}\tilde{\rho}\frac{D\tilde{\boldsymbol{v}}}{D\tilde{t}} = -\mathrm{ReEu}\tilde{\boldsymbol{\nabla}}\tilde{p} + \tilde{\boldsymbol{\nabla}} \cdot \tilde{\boldsymbol{\tau}}, \tag{1.13}$$

where St is the Strouhal number, Re is the Reynolds number, and Eu is the Euler number. The dissipative stress $\boldsymbol{\tau}$ is given by $\boldsymbol{\sigma} = -p\boldsymbol{I} + \boldsymbol{\tau}$. The tilded symbols denote the variables non-dimensionalized by the corresponding characteristic quantities. The definition of the dimensionless numbers are summarized in Table 1.2. The Lagrangian time derivative is explicitly given by

$$\mathrm{St}\frac{D}{D\tilde{t}} = \mathrm{St}\frac{\partial}{\partial\tilde{t}} + \tilde{\boldsymbol{v}} \cdot \tilde{\boldsymbol{\nabla}}. \tag{1.14}$$

Equations (1.12) and (1.13) can be simplified by ignoring the time derivative terms when the following conditions are satisfied, respectively:

$$\mathrm{St}\frac{\delta\rho_1}{\rho_0} \ll 1, \tag{1.15}$$

$$\mathrm{ReSt} \ll 1. \tag{1.16}$$

We estimate the characteristic density change as that in the adiabatic process, i.e., $\delta p_1 = c^2\delta\rho_1$, which leads to the expression for the density change rate as

$$\frac{\delta\rho_1}{\rho_0} = \mathrm{Ma}^2\mathrm{Eu}, \tag{1.17}$$

6

where Ma is the Mach number. When the condition Eq. (1.15) is satisfied, the fluid can be regarded as incompressible in the sense that the fluid density change is ignored. We will classify the fluid flows into quasi-steady and unsteady flows, according to the simplification of Eq. (1.13); then, in each case, we will derive the condition for the fluid incompressibility.

1.3.A Quasi-steady flow

When we are interested in the motion of dispersed particles in a steady flow or an external field such as gravity or a stationary electromagnetic field, the time scale of our observation t_o is equal to that of particle advection $\tau_{\mathrm{ad}} = a/V$, where V is the characteristic velocity in the system. In this case, the Strouhal number is St = 1. Because the pressure generates accompanied by the fluid flow, the Euler number is expected to be evaluated such that the pressure gradient term is comparable in magnitude to the dominant term in Eq. (1.13), i.e., Eu = $\max(\mathrm{Re}^{-1}, 1)$. Therefore, when we consider a slow flow such that Re $\ll$ 1, the momentum conservation law Eq. (1.13) is reduced to

$$-\boldsymbol{\nabla} p + \boldsymbol{\nabla} \cdot \boldsymbol{\tau} = 0, \tag{1.18}$$

which means that the fluid flow in this situation is steady. However, strictly speaking, this is not a true steady flow because the geometry of the particles varies with time; therefore, the fluid flow described in this situation is called a quasi-steady flow. In the quasi-steady flow, the particle motion is explicitly solved; however, the fluid motion is implicitly considered through the time-dependent boundary conditions imposed by the moving particles.

The condition for the fluid incompressibility in the quasi-steady flow is derived from Eqs. (1.15) and (1.17) with Eu = $\max(\mathrm{Re}^{-1}, 1)$ as

$$\mathrm{Ma} \ll \min(\sqrt{\mathrm{Re}}, 1). \tag{1.19}$$

When the fluid can be regarded as incompressible, the mass conservation law is reduced to the solenoidal condition expression for the fluid velocity field as

$$\boldsymbol{\nabla} \cdot \boldsymbol{v} = 0. \tag{1.20}$$

For an incompressible fluid, because the density deviation is not considered, the hydrodynamic equations are closed for the velocity field and only one thermodynamic quantity, namely the pressure. Therefore, the energy conservation does not need to be considered. The incompressibility condition Eq. (1.19) is satisfied for an ordinary low Reynolds number flow in a dispersion; therefore,

the dynamics of dispersion has been studied in the approximation of incompressible quasi-steady flow described by Eqs. (1.18) and (1.20).

1.3.B Unsteady flow

When we are interested in the dynamics of a dispersion in a flow changing in a small time scale such as a high frequency change caused by ultrasound, the time scale of interest t_o is comparable to that of the propagation process of hydrodynamic interactions, namely viscous diffusion τ_ν or sound propagation τ_c. In general, as shown in Fig. 1.1, τ_c is smaller than τ_ν; however, as described hereinbelow, such magnitude relation is not universal, and we give the time scale of our observation as $t_o = \max(\tau_\nu, \tau_c)$. In this case, the Strouhal number is given by $\mathrm{St} = \min(\mathrm{Re}^{-1}, \mathrm{Ma}^{-1})$, and Eq. (1.16) is not satisfied. Therefore, the time evolution of the fluid motion is explicitly solved in the hydrodynamic equations.

In this situation, the Euler number is expected to be $\mathrm{Eu} = \mathrm{St}$, and the condition for incompressibility is given by

$$\mathrm{MaSt} \ll 1, \tag{1.21}$$

which results in the condition for the time scale of the observation as $t_o \gg \tau_c$. Because the time scale of the observation is given by $t_o = \max(\tau_\nu, \tau_c)$, the fluid compressibility is significant when the time scale τ_ν is as well or smaller than τ_c. Introducing the compressibility factor as the ratio of the two time scales as

$$\varepsilon = \frac{\tau_c}{\tau_\nu} = \frac{\nu}{ac}, \tag{1.22}$$

the condition for fluid incompressibility in the unsteady flow is represented by $\varepsilon \ll 1$. The compressibility factor is quite small for dispersions with a typical fluid such as water or alcohol; for example, in a dispersion of water and particles of radius $a = 100\,\mathrm{nm}$, the compressibility factor is estimated to be $\varepsilon \approx 7 \times 10^{-3}$. However, because the speed of sound in a liquid does not largely depend on the material object, the compressibility factor can be as well or larger than 1 for highly viscous host fluid; for example, $\varepsilon \approx 0.7$ for olive oil and $\varepsilon \approx 10$ for corn syrup.

When we consider a compressible fluid, the energy conservation equation is required to close the hydrodynamic equations. However, in the studies presented in this dissertation, we adopt a simplification not to consider the energy conservation; that is, we assume a barotropic fluid

described by $p = p(\rho)$ such that

$$\boldsymbol{\nabla} p = c^2 \boldsymbol{\nabla} \rho. \tag{1.23}$$

With Eq. (1.23), the conservation equations of mass and momentum, i.e., Eqs. (1.1) and (1.2), are closed for velocity field $\boldsymbol{v}$ and two thermodynamic quantities ρ and p. To confirm the validity of this simplification, the entropy equation is examined. The entropy equation is derived from the hydrodynamic equations and is given in the non-dimensionized form by

$$\mathrm{ReSt}\tilde{\rho}\tilde{T}\frac{D\tilde{s}}{D\tilde{t}} = -\frac{1}{\mathrm{Pr}}\tilde{\boldsymbol{\nabla}} \cdot \tilde{\boldsymbol{q}} + \mathrm{Ec}\tilde{\boldsymbol{\tau}} : \tilde{\boldsymbol{\nabla}}\tilde{\boldsymbol{v}}, \tag{1.24}$$

where s is the entropy density, Pr is the Prandtl number, and Ec is the Eckert number. In a slow fluid flow, which is ordinary in a dispersion system, $\mathrm{Ec} \ll 1$ is satisfied; therefore, the entropy production is mostly due to the thermal conduction which is represented by the first term in the right-hand side of Eq. (1.24). The magnitude of the thermal conduction term is given by the inverse of the Prandtl number Pr; therefore, when Pr is sufficiently large, the fluid flow can be regarded as adiabatic in the observing time scale, and the entropy production is ignored. In this case, there are no entropy inhomogeneities, which lead to the thermodynamic relation of barotropic fluid Eq. (1.23). For typical fluids such as water or alcohol, the Prandtl number is at most 10. However, as with the compressibility factor, the Prandtl number becomes much larger for highly viscous fluid; for example, $\mathrm{Pr} \approx 10^3$ for olive oil and $\mathrm{Pr} \approx 10^4$ for corn syrup. Therefore, the validity of the assumption of barotropic fluid is enhanced with the increase in the fluid viscosity, or the compressibility factor.

1.4 Momentum transfer in a fluid

The equations describing the momentum transfer by two mechanisms, namely viscous diffusion and sound propagation, are respectively derived from the hydrodynamic equations. For sufficiently slow fluid flow, the hydrodynamic equations of Eqs. (1.1) and (1.2) can be linearized as follows:

$$\frac{\partial \rho}{\partial t} = -\rho_0 \boldsymbol{\nabla} \cdot \boldsymbol{v}, \tag{1.25}$$

$$\rho_0 \frac{\partial \boldsymbol{v}}{\partial t} = -\boldsymbol{\nabla} p + \eta \boldsymbol{\nabla}^2 \boldsymbol{v} + \left(\frac{1}{3}\eta + \eta_v\right) \boldsymbol{\nabla}\boldsymbol{\nabla} \cdot \boldsymbol{v}. \tag{1.26}$$

Taking rotation of both sides of Eq. (1.26), the temporal evolution of vorticity $\boldsymbol{\omega} = \nabla \times \boldsymbol{v}$ is obtained as the following diffusion equation:

$$\frac{\partial \boldsymbol{\omega}}{\partial t} = \nu \boldsymbol{\nabla}^2 \boldsymbol{\omega}. \tag{1.27}$$

9

On the other hand, taking divergence and time derivative of both sides of Eq. (1.26) and substituting Eq. (1.25) with assuming a barotropic fluid characterized by Eq. (1.23), the temporal evolution of expansion rate $\Theta = \nabla \cdot \boldsymbol{v}$ is obtained as the following damped wave equation:

$$\frac{\partial^2 \Theta}{\partial t^2} = c^2 \boldsymbol{\nabla}^2 \Theta + \nu_l \boldsymbol{\nabla}^2 \frac{\partial \Theta}{\partial t}, \tag{1.28}$$

where $\nu_l = (4/3)\nu + \eta_v/\rho_0$ is the longitudinal kinematic viscosity. Equations (1.27) and (1.28) describe the propagation of spinning motion and compression of fluid, respectively. The former corresponds to the momentum transfer by viscous diffusion, and the latter corresponds to that by sound propagation. The time scales governing these equations are obtained as τ_ν and τ_c, respectively. In this situation, the vorticity $\boldsymbol{\omega}$ and the expansion rate Θ propagates independently; however, when the flow is sufficiently fast, they are coupled through the non-linear advection term in the hydrodynamic equations.

1.5   Thesis objectives

In order to elucidate the influence of the fluid compressibility on the dynamics of dispersions, a few problems were investigated using direct numerical simulation. These subjects are as follows:

- Hydrodynamic interactions between particles in a compressible fluid

- Hydrodynamic interactions between a particle and walls in a compressible fluid

This dissertation is composed of five chapters as described below.

In **Chapter 2**, we present a direct numerical simulation method for investigating the dynamics of dispersed particles in a compressible solvent fluid. The validity of the simulation is examined by calculating the velocity relaxation of an impulsively forced spherical particle with a known analytical solution. The simulation also gives information about the fluid motion, which provides some insight into the particle motion. Fluctuations are also introduced by random stress, and the validity of this case is examined by comparing the calculation results with the fluctuation-dissipation theorem.

In **Chapter 3**, propagation process of hydrodynamic interactions by viscous diffusion and sound propagation is studied by direct numerical simulation. The hydrodynamic interactions for a system of two particles in a fluid are estimated by the velocity correlation of the particles. In an incompressible fluid, hydrodynamic interactions propagate instantaneously at the infinite speed of sound, followed by the temporal evolution of viscous diffusion. On the other hand, in a compressible

fluid, sound propagates at a finite speed, which affects the temporal evolution of the hydrodynamic interactions by the order of magnitude relation between the time scales of viscous diffusion and sound propagation. The hydrodynamic interactions are characterized by introducing the ratio of these time scales as an interactive compressibility factor.

In **Chapter 4**, The velocity relaxation of an impulsively forced spherical particle in a fluid confined by two parallel plane walls is studied using a direct numerical simulation approach. During the relaxation process, the momentum of the particle is transmitted in the ambient fluid by viscous diffusion and sound wave propagation, and the fluid flow accompanied by each mechanism has a different character and affects the particle motion differently. Because of the bounding walls, viscous diffusion is hampered, and the accompanying shear flow is gradually diminished. However, the sound wave is repeatedly reflected and spreads diffusely. As a result, the particle motion is governed by the sound wave and backtracks differently in a bulk fluid. The time when the backtracking of the particle occurs changes non-monotonically with respect to the compressibility factor given by Eq. (1.22) and is minimized at the characteristic compressibility factor. This factor depends on the wall spacing, and the dependence is different at small and large wall spacing regions based on the different mechanisms causing the backtracking.

In **Chapter 5**, the thesis is summarized.

References

1 W. B. Russel, D. A. Saville, and W. R. Schowalter, *Colloidal Dispersions*, (Cambridge University Press, Cambridge, UK, 1989).

2 J. Happel and H. Brenner, *Low Reynolds Number Hydrodynamics*, (Kluwer Academic, Boston, 1983).

3 S. Kim and S. J. Karrila, *Microhydrodynamics*, (Butterworth-Heinemann, Boston, 1991).

4 J. Rotne and S. Prager, J. Chem. Phys. **50**, 4831 (1969).

5 H. Yamakawa, J. Chem. Phys. **53**, 436 (1970).

6 D. L. Ermak and J. A. McCammon, J. Chem. Phys. **69**, 1352 (1978).

7 J. F. Brady and G. Bossis, Annu. Rev. Fluid Mech. **20**, 111 (1988).

8 J. T. Padding and A. A. Louis, Phys. Rev. E **74** 031402 (2006).

9 A. J. C. Ladd, J. Fluid Mech. **271**, 285 (1994).

10 H. H. Hu, N. A. Patankar, and M. Y. Zhu, J. Comput. Phys. **192**, 427 (2001).

11 H. Tanaka and T. Araki, Phys. Rev. Lett. **85**, 1338 (2000).

12 Y. Nakayama and R. Yamamoto, Phys. Rev. E **71**, 036707 (2005).

13 J. P. Hansen and I. R. McDonald: *Theory of Simple Liquids* (Academic, London, 2006) 3rd ed., Chap. 8.

Chapter 2

Direct numerical simulation of dispersed particles in a compressible fluid

2.1 Introduction

Particle dispersions have various unique properties, and an understanding of these properties is important in many fields of science and engineering. These properties originate from the dynamics of particles, which are extremely complicated because of the hydrodynamic interactions among particles mediated by the motion of the surrounding fluid. Therefore, several numerical approaches have been formulated to investigate the dynamics of such dispersions. As one of these approaches, a direct numerical simulation has been developed, wherein the hydrodynamic interactions are directly computed by simultaneously solving for the motion of the fluid and the motion of the particle. In recent years, we have developed an efficient direct numerical simulation scheme for dispersions, which is called the smoothed profile method (SPM).[1,2] In this scheme, the sharp interface between the fluid and the particles is replaced by a smoothed interface using a continuous profile function. The Navier-Stokes equations are solved for the fluid motion on a fixed square grid, and Newton's and Euler's equations of motion for the particles are solved simultaneously while considering the momentum exchange between the fluid and the particles.

The hydrodynamic interactions are transmitted in two ways: via viscous momentum diffusion and via sound propagation. The time scale of viscous diffusion over the particle size is $\tau_\nu = a^2/\nu$, and that of sound propagation is $\tau_c = a/c$, where a is the particle radius, ν is the kinematic viscosity, and c is the speed of sound in the fluid. Here, we will define the compressibility factor as the ratio of the two time scales:

$$\varepsilon = \frac{\tau_c}{\tau_\nu} = \frac{\nu}{ac}.$$

(2.1)

This factor represents the degree of influence of compressibility in the dynamics of the dispersed particles. According to Eq. (2.1), the compressibility becomes increasingly important as the particle size decreases. Indeed, the compressibility of a system has been considered an important factor in molecular scale dynamics of monatomic liquids studied using hydrodynamic theories.[3,4]

On the other hand, in studies of particle dispersions, compressibility has rarely been considered, and an incompressible host fluid is generally assumed. In the case of a dispersed particle of radius $a = 100\,\mathrm{nm}$ in water, for instance, the compressibility factor is evaluated from $\nu = 1.0 \times 10^{-6}\,\mathrm{m^2/s}$ and $c = 1.5 \times 10^3\,\mathrm{m/s}$ to be $\varepsilon = 6.7 \times 10^{-3}$. In many cases, researchers are interested in phenomena progressing over the time scale of viscous diffusion or even longer time scales, such as those relating to shear properties, electrophoresis, and sedimentation. Therefore, the assumption of an incompressible host fluid is valid, and most direct numerical simulation methods, including SPM, have been developed on the premise of incompressible fluids. However, when we investigate phenomena associated with sound propagation, such as sonic agglomeration, acoustic spectroscopy, and electroacoustic measurements, the consideration of compressibility is required.

In the present study, we extend the SPM to compressible fluids. Some aspects of the dynamics of a single particle in a compressible fluid have been theoretically analyzed,[3–7] and we compare the simulation results obtained herein with analytical solutions to determine the accuracy of the simulation. In particular, we consider the velocity relaxation of a spherical particle after an impulsive force is added. The numerical simulation also gives information regarding fluid motion for which the analytical solution is unknown, and the dynamics of the particle can be investigated from the viewpoint of the fluid dynamics. In addition, we also consider a system with thermal fluctuations by introducing random stress, and the velocity autocorrelation function is compared with the analytical solution according to the fluctuation-dissipation theorem.

2.2 Simulation Method

2.2.A Equations

In the SPM, the particle-fluid boundary is replaced by a continuous interface. For this purpose, the smoothed profile function $\phi(\boldsymbol{r}, t) \in [1, 0]$ is introduced. This function represents the boundary between the fluid and particle regions: $\phi = 1$ at the particle domain, and $\phi = 0$ at the fluid domain. The two regions are smoothly connected through thin interfacial regions with a thickness characterized by ξ. The mathematical expression of ϕ can be found in a previous paper.[1] The total velocity field is defined as

$$\boldsymbol{v} = (1 - \phi)\boldsymbol{v}_f + \phi\boldsymbol{v}_p, \tag{2.2}$$

14

where $\boldsymbol{v}_f(\boldsymbol{r}, t)$ is the fluid velocity field, and $\boldsymbol{v}_p(\boldsymbol{r}, t)$ is the particle velocity field constructed from rigid motions of the particles.[1,2] When a compressible host fluid is considered, the fluid mass density is altered, and we define the mass density field as

$$\rho_f = (1 - \phi)\rho. \tag{2.3}$$

The auxiliary mass density field $\rho(\boldsymbol{r}, t)$ is defined over the entire domain. However, the physical fluid mass density $\rho_f(\boldsymbol{r}, t)$ must be zero within the particle domain, and this requirement is satisfied by multiplying by $(1 - \phi)$.

The equations governing the dynamics of the dispersion system are given as hydrodynamic equations with the addition of a body force. The hydrodynamic equations consist of three conservation laws concerning mass, momentum, and energy. The conservation equations of mass and momentum are given as

$$\frac{\partial \rho}{\partial t} + \boldsymbol{\nabla} \cdot \boldsymbol{m} = 0, \tag{2.4}$$

$$\frac{\partial \boldsymbol{m}}{\partial t} + \boldsymbol{\nabla} \cdot (\boldsymbol{m}\boldsymbol{v}) = \boldsymbol{\nabla} \cdot \boldsymbol{\sigma} + \rho\phi\boldsymbol{f}_p, \tag{2.5}$$

where $\boldsymbol{m}(\boldsymbol{r}, t) = \rho(\boldsymbol{r}, t)\boldsymbol{v}(\boldsymbol{r}, t)$ is the momentum density field. We consider a compressible Newtonian fluid, and the stress tensor is given by

$$\boldsymbol{\sigma} = -p\boldsymbol{I} + \eta[\boldsymbol{\nabla}\boldsymbol{v} + (\boldsymbol{\nabla}\boldsymbol{v})^T] + \left(\eta_v - \frac{2}{3}\eta\right)(\boldsymbol{\nabla} \cdot \boldsymbol{v})\boldsymbol{I}, \tag{2.6}$$

where $p(\boldsymbol{r}, t)$ is the pressure, η is the shear viscosity, and η_v is the bulk viscosity. A body force $\rho\phi\boldsymbol{f}_p$ is added so that the rigidity of the particles is satisfied. Additionally, we assume a barotropic fluid described by $p = p(\rho)$, and the pressure gradient is proportional to that of the mass density:

$$\boldsymbol{\nabla}p = c^2\boldsymbol{\nabla}\rho. \tag{2.7}$$

Equations (2.4)-(2.7) are closed for the variables ρ, $\boldsymbol{m}$, and p; therefore, energy conservation does not need to be considered.

The motion of the dispersed particles is governed by Newton's and Euler's equations of motion:

$$M_i\frac{\mathrm{d}}{\mathrm{d}t}\boldsymbol{V}_i = \boldsymbol{F}_i^H + \boldsymbol{F}_i^C, \quad \frac{\mathrm{d}}{\mathrm{d}t}\boldsymbol{R}_i = \boldsymbol{V}_i, \tag{2.8}$$

$$\boldsymbol{I}_i \cdot \frac{\mathrm{d}}{\mathrm{d}t}\boldsymbol{\Omega}_i = \boldsymbol{N}_i^H, \tag{2.9}$$

15

where $\boldsymbol{R}_i$, $\boldsymbol{V}_i$, and $\boldsymbol{\Omega}_i$ are the position, translational velocity, and rotational velocity of the i-th particle, respectively. The particle has a mass M_i and a moment of inertia $\boldsymbol{I}_i$. The hydrodynamic force $\boldsymbol{F}_i^H$ and torque $\boldsymbol{N}_i^H$ are exerted on the particle by the fluid, and the force $\boldsymbol{F}_i^C$ is exerted through direct interactions among the particles.

The effect of thermal fluctuations on the dynamics of particles is important when the particle size is on the order of a micrometer or smaller. Fluctuations are introduced through a random stress tensor $\boldsymbol{s}$, which is added in Eq. (2.6). The random stress is a stochastic variable satisfying the fluctuation-dissipation relation:[8]

$$\langle s_{ij}(\boldsymbol{r}, t) s_{kl}(\boldsymbol{r}', t') \rangle = 2 k_B T \eta_{ijkl} \delta(\boldsymbol{r}' - \boldsymbol{r}) \delta(t' - t), \tag{2.10}$$

where k_B is the Boltzmann constant, T is the temperature, and

$$\eta_{ijkl} = \eta(\delta_{ik}\delta_{jl} + \delta_{il}\delta_{jk}) + \left(\eta_v - \frac{2}{3}\eta \right) \delta_{ij}\delta_{kl}. \tag{2.11}$$

Brownian motion of the dispersed particles is induced by random stress acting on the fluid. Thermal fluctuations can be introduced using the Langevin approach, where random forces are exerted on the particles.[9] However, this approach does not accurately represent the short-time dynamics of the system because the time autocorrelation of the hydrodynamic force acting on the particles is neglected. Therefore, the fluctuating hydrodynamics approach is more appropriate for investigating dynamics over the time scale of sound propagation.

2.2.B   Simulation procedure

Here, the time-discretized evolution of the equations is derived. The time step t_n represents the n-th discretized time, and the time step change from t_n to $t_{n+1} = t_n + h$ will be considered. The time evolution of the system is determined through the following steps:

(i) The mass and momentum density changes associated with sound propagation are calculated as

$$\rho^{n+1} = \rho^n - \int_{t_n}^{t_n+h} dt \boldsymbol{\nabla} \cdot \boldsymbol{m}, . \tag{2.12}$$

$$\boldsymbol{m}^* = \boldsymbol{m}^n - c^2 \int_{t_n}^{t_n+h} dt \boldsymbol{\nabla} \rho. \tag{2.13}$$

When we assume a periodic boundary condition and use the Fourier spectral method, a semi-implicit scheme becomes feasible.[10] This situation eases the restriction on the time increment for a small compressibility factor ε.

(ii) The time evolution of the advection and viscous diffusion terms are calculated as

$$\boldsymbol{m}^{**} = \boldsymbol{m}^* + \int_{t_n}^{t_n+h} dt \boldsymbol{\nabla} \cdot (\boldsymbol{\tau} - \boldsymbol{m}\boldsymbol{v}), \tag{2.14}$$

where $\boldsymbol{\tau}$ is the dissipative stress given by $\boldsymbol{\sigma} = -p\boldsymbol{I} + \boldsymbol{\tau}$.

(iii) In concert with the advection of the particle domain, the position of each dispersed particle evolves as

$$\boldsymbol{R}_i^{n+1} = \boldsymbol{R}_i^n + \int_{t_n}^{t_n+h} dt \boldsymbol{V}_i. \tag{2.15}$$

(iv) The hydrodynamic force and torque are derived by considering the conservation of momentum. The time-integrated hydrodynamic force and torque are computed as

$$\int_{t_n}^{t_n+h} dt \boldsymbol{F}_i^H = \int d\boldsymbol{r} \phi_i^{n+1} (\boldsymbol{m}^{**} - \rho^{n+1} \boldsymbol{v}_p^n), \tag{2.16}$$

$$\int_{t_n}^{t_n+h} dt \boldsymbol{N}_i^H = \int d\boldsymbol{r} [(\boldsymbol{r} - \boldsymbol{R}_i^{n+1}) \times \phi_i^{n+1} (\boldsymbol{m}^{**} - \rho^{n+1} \boldsymbol{v}_p^n)]. \tag{2.17}$$

With these and other forces acting on the particles, the translational and rotational velocity of each dispersed particle evolve as

$$\boldsymbol{V}_i^{n+1} = \boldsymbol{V}_i^n + M_i^{-1} \int_{t_n}^{t_n+h} dt (\boldsymbol{F}_i^H + \boldsymbol{F}_i^C), \tag{2.18}$$

$$\boldsymbol{\Omega}_i^{n+1} = \boldsymbol{\Omega}_i^n + \boldsymbol{I}_i^{-1} \cdot \int_{t_n}^{t_n+h} dt \boldsymbol{N}_i^H. \tag{2.19}$$

(v) The updated velocity of the particle region is imposed on the velocity field as the body force $\rho \phi \boldsymbol{f}_p$.

$$\boldsymbol{m}^{n+1} = \boldsymbol{m}^{**} + \int_{t_n}^{t_n+h} dt \rho \phi \boldsymbol{f}_p, \tag{2.20}$$

$$\int_{t_n}^{t_n+h} dt \rho \phi \boldsymbol{f}_p = \phi^{n+1} (\rho^{n+1} \boldsymbol{v}_p^{n+1} - \boldsymbol{m}^{**}). \tag{2.21}$$

In the case of an incompressible fluid, the pressure is spontaneously determined by the solenoidal condition of the velocity field. On the other hand, in the present case, the pressure or mass density varies independently of the velocity field.

2.3 Simulation Results

Numerical simulations are performed for a three-dimensional box with periodic boundary conditions. The space is divided by meshes of length Δ, which is the unit length. The units of the other physical quantities are defined by combining $\eta = 1$ and $\rho_0 = 1$ with Δ, where ρ_0 is the fluid mass density at equilibrium. The system size is $L_x \times L_y \times L_z = 128 \times 128 \times 128$. The other parameters are set as $a = 4$, $\xi = 1$, $\rho_p = 1$, $\eta_v = 0$, and $h = 0.01$, where ρ_p is the particle mass density. We performed simulations of the dynamics of an isolated spherical particle in a fluid in two situations. First, we investigated the relaxation response of a particle with an impulsive force. Second, we consider the velocity autocorrelation function of a particle with thermal fluctuations.

Because the input particle radius $a = 4$ is not necessarily equal to the effective hydrodynamic radius a^* of the particle represented by the smoothed profile function ϕ with a fuzzy interface of thickness ξ, we calculated a^* from the drag force acting on the spherical particle moving at velocity V, which is analytically given by $F_D = 6\pi\eta a K(\phi)V$, where $K(\phi)$ represents the effect of the periodic boundary condition depending on the volume fraction of the particle ϕ.[11] The effective radius was evaluated as $a^* = 3.87$ in the present simulations, and therefore, the momentum diffusion time is estimated to be $\tau_\nu = a^{*2}/\nu$ in this case. When we compare the present simulation results with the analytical solutions, the corrected particle density $\rho_p^* = (a^*/a)^3 \rho_p$ and the compressibility factor $\varepsilon^* = (a/a^*)\varepsilon$ of the analytical solutions are employed.

2.3.A Relaxation

Let us consider a single spherical particle in a fluid at rest. We will investigate the relaxation of the particle velocity after exerting an impulsive force at the center of the particle. The impulsive force is assumed to be small; in other words, we will consider the motion of the particle and the fluid for low Reynolds and Mach numbers. We set the impulsive force to achieve an initial particle Reynolds number of $\mathrm{Re_p} = 0.01$. Here, we introduce the velocity relaxation function as the normalized velocity change of the particle as

$$\boldsymbol{V}(t) = \frac{\boldsymbol{P}}{M}\gamma(t), \tag{2.22}$$

where $\boldsymbol{P}$ is the impulsive force added at $t = 0$. The analytical form of the relaxation function is obtained from a Stokes approximation (see the Appendix).

The simulations are performed with compressibility factors of $\varepsilon = 0.1$, 0.6, 1.0, and 1.5. The
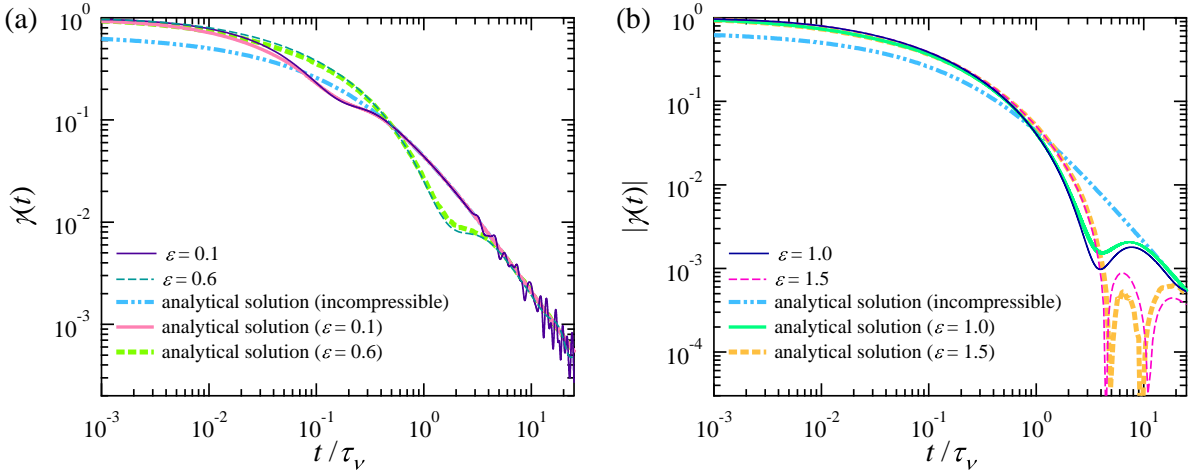
Figure 2.1: The velocity relaxation function for various compressibility factors: (a) $\varepsilon = 0.1$, 0.6, (b) 1.0, and 1.5. The bold lines illustrate the analytic solutions for various compressibility factors, and the bold dashed double-dotted line shows the analytic solution for an incompressible fluid.

condition $\varepsilon > 1$ implies that the sound propagation occurs more slowly than the viscous diffusion, according to the definition given in Eq. (2.1). The simulation results agree quite well with the analytical solutions for all of the compressibility factors ε, as shown in Fig. 2.1. The oscillation of $t/\tau_\nu \gtrsim 2$ at $\varepsilon = 0.1$ arises from the periodic boundary conditions. In this case, the sound pulse arrives at the end of the system at $t/\tau_\nu = 1.6$; afterward, the sound pulse returns and affects the particle motion.

The velocity relaxation results highlight some remarkable properties of dynamics in a compressible fluid. In the case of an incompressible fluid, part of the particle momentum is instantly carried away by the propagation of the infinite-speed sound wave, and the particle moves as if its mass were $M^* = M + M_f/2$, where $M_f = 4\pi a^3 \rho_0/3$ is the mass of the displaced fluid.[12] Therefore, the velocity relaxation function for an incompressible fluid at the initial time is $\gamma(+0) = M/M^*$; afterward, the particle velocity gradually decreases because of momentum diffusion in the fluid caused by its viscosity. Eventually, this decay obeys the power law $t^{-3/2}$ in the long-time region. On the other hand, in the case of a compressible fluid, the velocity relaxation function indicates that the relaxation due to sound propagation occurs in a finite time interval. For the compressibility factor $\varepsilon < 1$, the two relaxation processes are almost separate, and the relaxation function coincides with that of an incompressible fluid after the relaxation due to the sound propagation occurs. With an increase in the compressibility factor, nonmonotonic behavior is observed in the relaxation function, and finally, inversion of the particle velocity is observed, as shown in the investigation of the
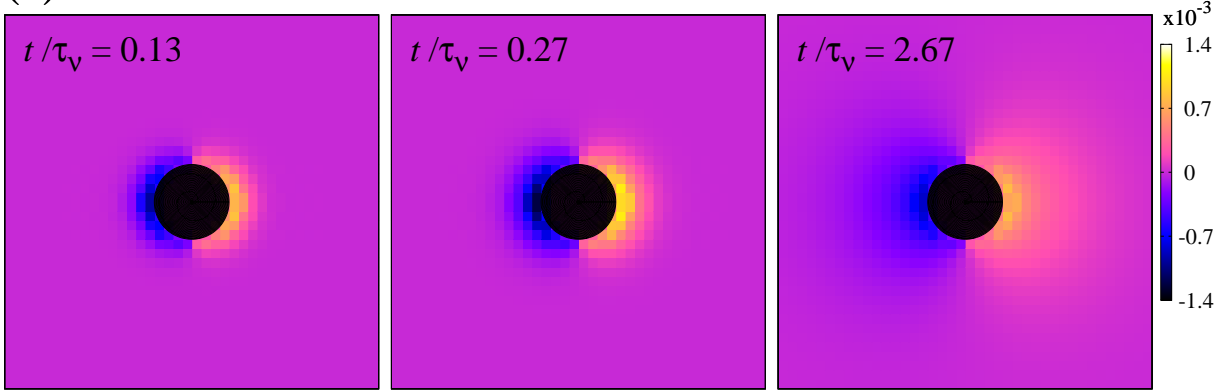
19
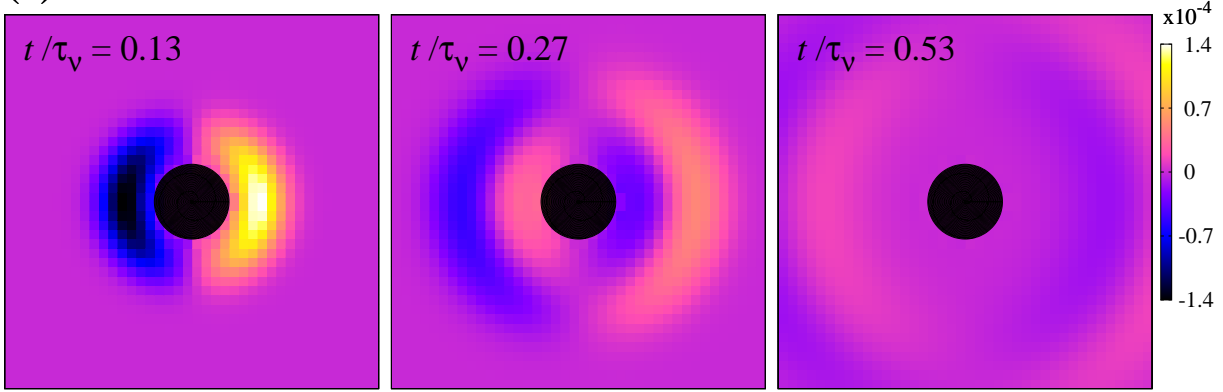
Figure 2.2: Time evolution of the fluid density deviation around the particle. The compressibility factors are (a) $\varepsilon = 0.1$ (upper row) and (b) $\varepsilon = 1.5$ (lower row). The color scale represents negative (darker) to positive (lighter) density deviation. The black circle represents the particle. The direction of the initial particle velocity is right in these pictures.

analytical solution.[7]

The density deviation around the particle is shown in Fig. 2.2, for which an analytical form has not been obtained. For a small compressibility $\varepsilon = 0.1$, the sound wave pulse expands from the particle very quickly, which corresponds to a rapid decrease in the particle momentum due to sound propagation. On the other hand, for a large compressibility $\varepsilon = 1.5$, the sound pulse does not spread. The pulse remains within the vicinity of the particle and gradually decays through viscous diffusion. The continuation of high fluid density in front of the particle is expected to cause backtracking motion.

The velocity field around the particle is also affected by the compressibility. The velocity field can be formally decomposed into two components: an incompressible (solenoidal) component $\boldsymbol{v}^{\mathrm{I}}$ and a compressible component $\boldsymbol{v}^{\mathrm{C}}$. The former is a solenoidal vector field when $\boldsymbol{\nabla} \cdot \boldsymbol{v}^{\mathrm{I}} = 0$, and the latter is an irrotational vector field when $\boldsymbol{\nabla} \times \boldsymbol{v}^{\mathrm{C}} = 0$. Therefore, the divergence of the
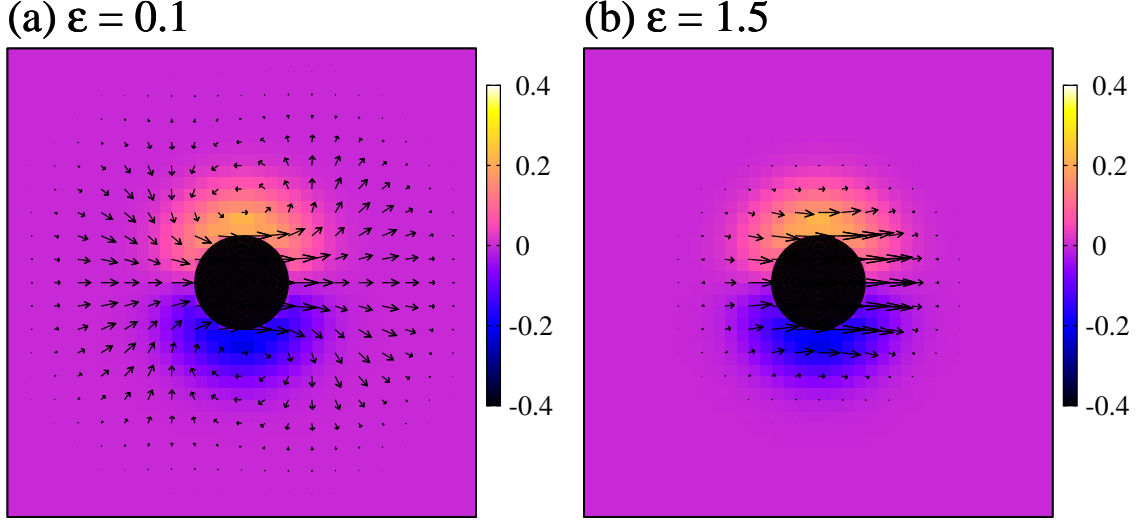
(a) ε = 0.1   (b) ε = 1.5

Figure 2.3: The fluid velocity field and its rotation, $\boldsymbol{\nabla} \times \boldsymbol{v}$, at $t/\tau_\nu = 0.27$. The values are normalized by the factor $Ma^*/|\boldsymbol{P}|$. The component normal to the figure plane is depicted. The compressibility factors are (a) $\varepsilon = 0.1$ and (b) $\varepsilon = 1.5$. The color scale represents negative (darker) to positive (lighter) rotation. The black circle represents the particle. The direction of the initial particle velocity is right in these pictures.

velocity field $\boldsymbol{\nabla} \cdot \boldsymbol{v}$ gives information regarding the compressible component, and the rotation of the velocity field $\boldsymbol{\nabla} \times \boldsymbol{v}$ gives information pertaining to the incompressible component. The rotation and divergence of the velocity field are shown in Figs. 2.3 and 2.4, respectively. The velocity field is also depicted in these figures. An obvious vortex ring is observed around the particle for a small compressibility $\varepsilon = 0.1$, while the vortex ring is not clear for a large compressibility $\varepsilon = 1.5$. The rotation corresponds to the intensity of the vorticity, and the map in Fig. 2.3 represents a pair of vortex rings that is inherent to an incompressible fluid.[13] The rotation remains nearly constant, regardless of the compressibility, which indicates that the incompressible component is not affected by the compressibility. The vector fields $\boldsymbol{v}^{\mathrm{I}}$ and $\boldsymbol{v}^{\mathrm{C}}$ influence each other only through the nonlinear terms in Eqs. (2.4) and (2.5); however, in the present simulations, a low Reynolds number flow is assumed, and the additivity of the incompressible and compressible components is almost valid. Therefore, the effect of compressibility is observed only from the divergence of the velocity field depicted in Fig. 2.4. The region of positive divergence represents the source of the flow, and the negative region represents the sink of the flow. From the equation of continuity Eq. (2.4), the divergence is equal to the reverse sign of the time change rate of the mass density:

$$\boldsymbol{\nabla} \cdot \boldsymbol{v} = -\frac{D}{Dt} \ln \frac{\rho}{\rho_0}. \tag{2.23}$$

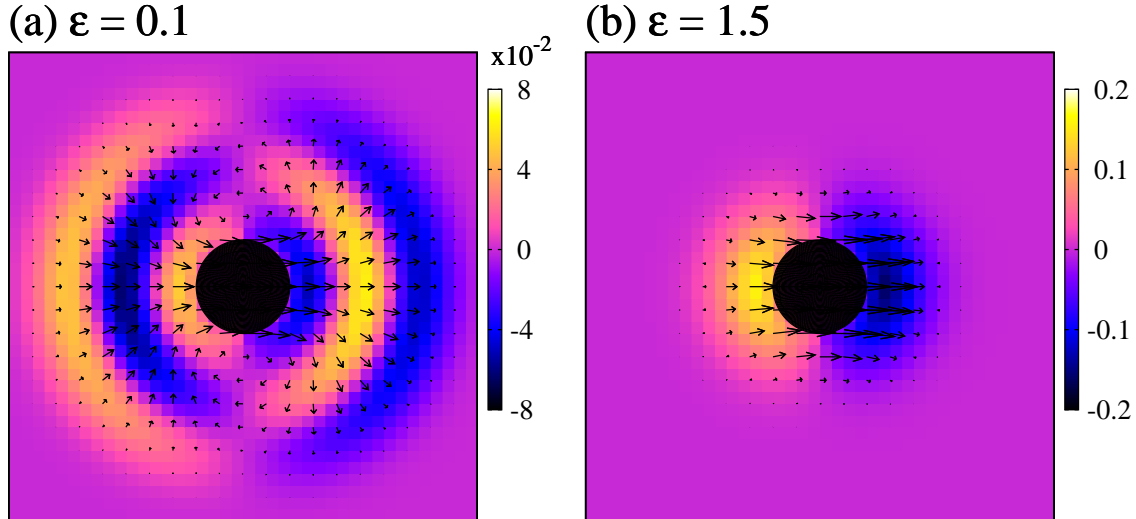According to this relation, the source corresponds to the density decrease and the sink corresponds

Figure 2.4: The fluid velocity field and its divergence, $\boldsymbol{\nabla} \cdot \boldsymbol{v}$, at $t/\tau_\nu = 0.27$. The values are normalized by the factor $Ma^*/|\boldsymbol{P}|$. The compressibility factors are (a) $\varepsilon = 0.1$ and (b) $\varepsilon = 1.5$. The color scale represents negative (darker) to positive (lighter) divergence. The black circle represents the particle. The direction of the initial particle velocity is right in these pictures.

to the density increase. Therefore, the source and the sink move according to the sound propagation. The propagation speed decreases with increasing compressibility, which corresponds to the difference in Fig. 2.4 related to the compressibility. The pattern of the total velocity field is described as the superposition of the vortex convection of the incompressible component $\boldsymbol{v}^{\mathrm{I}}$ and the source-sink flow of the compressible component $\boldsymbol{v}^{\mathrm{C}}$. The compressibility factor governs the relative time evolution of each component to produce various flow patterns.

2.3.B   Fluctuation

Thermal fluctuations are introduced through random stress in the host fluid. Computationally, a random stress term satisfying Eq. (2.10) is added to the stress tensor given by Eq. (2.6). We consider a single particle in the fluid, which moves randomly as a result of thermal fluctuations. From the fluctuation-dissipation theorem, the velocity autocorrelation function of the particle is related to the relaxation function as

$$\gamma(t) = \frac{M}{3k_B T}\langle \boldsymbol{V}(0) \cdot \boldsymbol{V}(t)\rangle. \tag{2.24}$$

The accuracy of the fluctuating system can be confirmed by the validity of this relation. In the numerical procedure for solving a stochastic differential equation, the numerical error can be larger than that in an ordinary differential equation due to the truncation error in the time integration of the random noise term.[14] This error is decreased with the decrease in the time increment, and
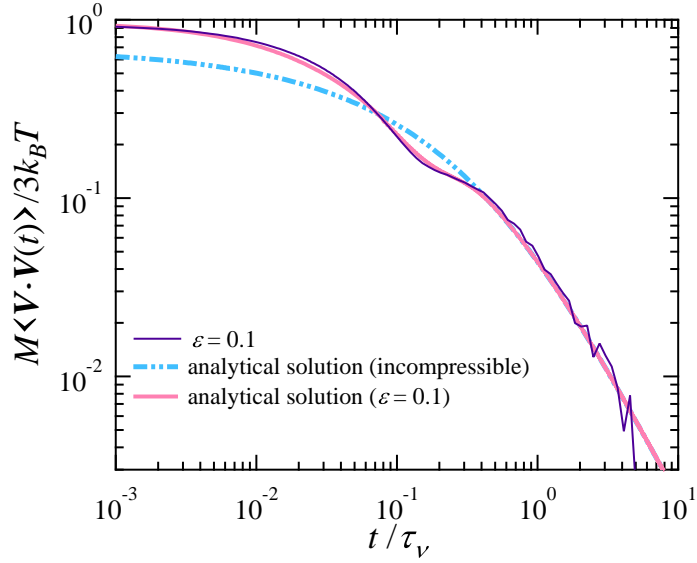
Figure 2.5: (Color online) The velocity autocorrelation function at $\varepsilon = 0.1$ and $k_B T = 10^{-4}$. The bold solid line represents the analytic solution of the velocity relaxation function. The bold dashed double-dotted line shows the analytic solution for an incompressible fluid.

we set the smaller time increment than that in the relaxation case as $h = 0.01$. The system size is therefore scaled down to $L_x \times L_y \times L_z = 64 \times 64 \times 64$ to compensate the increased computational demand due to the small h explained above. The simulation results for $\varepsilon = 0.1$ are shown in Fig. 2.5, which shows good agreement with the analytical solution of the relaxation function. The consistency between the input and calculated temperatures is also tested. We can evaluate the temperature from the average kinetic energy of a fluid or a particle, i.e., $k_B T_f = \Delta^3 \langle \rho \boldsymbol{v}^2 \rangle / 3$ or $k_B T_p = M \langle \boldsymbol{V}^2 \rangle / 3$. We evaluated these two temperatures as the ratio to the input temperature T. From the fluid motion, the temperature was evaluated as $T_f / T = 1.06$, while that of the particle motion was $T_p / T = 0.93$. The overestimation of the fluid temperature T_f is simply due to the truncation error in the time integration of the stochastic differential equation. On the other hand, the particle temperature T_p is slightly below the input temperature T. This discrepancy is considered to be due to the small numerical inaccuracy introduced in treating the momentum transfer through the particle-fluid interface using the SPM. Further improvements on the treatments of fluctuations in the particle-fluid interfacial region will be discussed in the future.

2.4 Conclusion

We extended the SPM to particle dispersions in compressible fluids. The validity of the method was confirmed by calculating the velocity relaxation function of a single spherical particle in a compressible fluid. The effect of compressibility on the velocity relaxation was also observed, showing two-stage relaxation in a low-compressibility fluid and backtracking motion in a high-compressibility fluid. These particle motions were considered by investigating the fluid density deviation. The propagation of the sound pulse around the particle is governed by the compressibility, and the influence of the sound disappears in a low-compressibility fluid but is maintained in a high-compressibility fluid. The effect of compressibility on the fluid velocity field was also observed, which was essentially understood to arise from changes in the time evolution of the source-sink flow component caused by the compressibility.

A simulation of the motion of a single spherical particle in a fluctuating fluid was also performed. The calculated velocity autocorrelation function of the particle showed good agreement with the analytical solution of the relaxation function, and the validity of the fluctuation-dissipation theorem was confirmed.

Appendix: Velocity Relaxation of a Particle in a Compressible Fluid

The equation of motion for a spherical particle under an external force $\boldsymbol{E}(t)$ in a compressible fluid can be expressed by the linear response theory as

$$M\frac{\mathrm{d}}{\mathrm{d}t}\boldsymbol{V} = -\int_{-\infty}^{t} \mathrm{d}s\zeta(t-s)\boldsymbol{V}(s) + \boldsymbol{E}(t), \tag{2.25}$$

where $\zeta(t)$ is the memory kernel of the friction force. The memory kernel is analytically expressed in frequency representation. Assuming a stick boundary condition on the surface of the sphere, the memory kernel is obtained from the linearized hydrodynamic equations (Stokes approximation) as[5,6]

$$
\begin{aligned}
\hat{\zeta}(\omega) &= \int_{-\infty}^{\infty} \zeta(t)e^{i\omega t}\mathrm{d}t, \\
&= \frac{4\pi}{3}\eta a x^2 \frac{(1+x)(9-9iy-2y^2)+x^2(1-iy)}{2x^2(1-iy)-(1+x)y^2-x^2y^2},
\end{aligned}
\tag{2.26}
$$

with

$$x = a(-i\omega\rho_0/\eta)^{1/2}, \quad y = a\omega/\tilde{c}, \tag{2.27}$$

24

and

$$\tilde{c} = \left[c^2 - \frac{i\omega}{\rho_0} \left(\frac{4}{3}\eta + \eta_v \right) \right]^{1/2}. \tag{2.28}$$

According to Eq. (2.25), the particle velocity is linearly dependent on the external force in frequency representation:

$$\hat{\boldsymbol{V}}(\omega) = \hat{\Gamma}(\omega)\hat{\boldsymbol{E}}(\omega), \tag{2.29}$$

where the admittance $\hat{\Gamma}(\omega)$ is given by

$$\hat{\Gamma}(\omega) = [-i\omega M + \hat{\zeta}(\omega)]^{-1}. \tag{2.30}$$

In the case that an impulsive force is exerted on the sphere, the external force in frequency representation is given as a constant vector $\hat{\boldsymbol{E}}(\omega) = \boldsymbol{P}$, and the velocity relaxation function is given by $\gamma(t) = M\Gamma(t)$ according to Eq. (2.22).

References

1 Y. Nakayama and R. Yamamoto, Phys. Rev. E **71**, 036707 (2005).

2 Y. Nakayama, K. Kim, and R. Yamamoto, Eur. Phys. J. E **26**, 361 (2008).

3 R. Zwanzig and M. Bixon, Phys. Rev. A **2**, 2005 (1970).

4 H. Metiu, D. W. Oxtoby, and K. F. Freed, Phys. Rev. A **15**, 361 (1977).

5 D. Bedeaux and P. Mazur, Physica **78**, 505 (1974).

6 B. U. Felderhof, Phys. Fluids **19**, 126101 (2007).

7 B. U. Felderhof, J. Chem. Phys. **123**, 044902 (2005).

8 L. D. Landau and E. M. Lifshitz, *Fluid Mechanics* (Pergamon, London, 1959).

9 T. Iwashita, Y. Nakayama, and R. Yamamoto, J. Phys. Soc. Jpn. **77**, 074007 (2008).

10 G. Erlebacher, M. Y. Hussaini, H. O. Kreiss, and S. Sarkar, Theor. Comput. Fluid. Dyn. **2**, 73 (1990).

11 H. Hashimoto, J. Fluid Mech. **5**, 317 (1959).

12 R. Zwanzig and M. Bixon, J. Fluid. Mech. **69**, 21 (1975).

13 B. U. Felderhof, Phys. Fluids **19**, 073102 (2007).

14 R. L. Honeycutt, Phys. Rev. A **45**, 600 (1992).

Chapter 3

Propagation of hydrodynamic interactions between particles in a compressible fluid

3.1 Introduction

In particle dispersions, the motion of each particle in a fluid solvent affects the motion of the other particles. Such dynamical interactions are called hydrodynamic interactions; these interactions produce complex dynamical behavior for dispersions, which can be observed in particle aggregation and sedimentation phenomena.

Here, hydrodynamic interactions correspond to momentum exchange among particles through the ambient fluid. Hydrodynamic interactions are transmitted by two mechanisms: viscous diffusion and sound propagation. These two mechanisms occur at different time scales. The time scale for viscous diffusion over a distance equal to the particle size is $\tau_\nu = a^2/\nu$, while the time scale for sound propagation is $\tau_c = a/c$, where a is the particle radius, ν is the kinematic viscosity, and c is the speed of sound in the fluid. To study dynamical effects at the particle size scale, the relative significance of the sound propagation mechanism in hydrodynamic interactions can be assessed from the ratio of the two time scales described above:

$$\varepsilon = \frac{\tau_c}{\tau_\nu} = \frac{\nu}{ac}. \tag{3.1}$$

This dimensionless quantity is called the compressibility factor. Because sound propagation is much faster than viscous diffusion, the compressibility factor is generally quite small; for example, in a dispersion of water and particles of radius $a = 100 \, \text{nm}$, the compressibility factor is estimated to be $\varepsilon \approx 7 \times 10^{-3}$. In this case, the assumption of incompressibility is fully justified. Thus, fluids are assumed to be incompressible in many theoretical studies of hydrodynamic interactions and viscous diffusion is only considered in temporal evolution mechanisms for hydrodynamic interactions .[1,2] On the other hand, the speed of sound in a liquid is around 10^3 m/s irrespective of the liquid considered, producing a large compressibility factor for a dispersion of a highly viscous fluid solvent; for example, $\varepsilon \approx 0.7$ for olive oil and $\varepsilon \approx 10$ for corn syrup.

In recent years, the temporal evolution of hydrodynamic interactions between two particles

has been directly observed.[3–6] In these experimental studies, particles were trapped by optical tweezers and the correlations between the positional fluctuations of particles were measured. The authors reported the temporal evolution of hydrodynamic interactions in the viscous diffusion regime, which coincided with analytical predictions that assumed the fluid was incompressible. Evidence for hydrodynamic interactions by sound propagation was also observed,[3,7,8] but could not be captured due to the extremely short time scale of sound propagation.

In the present study, we investigate the propagation process of hydrodynamic interactions using direct numerical simulation. Within this approach, the hydrodynamic interactions are directly computed by simultaneously solving for the motions of the fluid and the particles with appropriate boundary conditions. We use the smoothed profile method (SPM),[9,10] which can be applied to a compressible fluid as well as an incompressible fluid.[11] With considering the fluid compressibility, sound propagation can be captured.

We consider a system of two particles in a fluid and investigate the correlated motion of the particles. In particular, we estimate the velocity relaxation of the particle in response to the exertion of an impulsive force on the other particle. This velocity cross-relaxation function is equivalent to the velocity cross-correlation function from the fluctuation-dissipation theorem. The numerical results for the velocity cross-relaxation function may be interpreted in terms of the temporal evolution of the flow field around the particle. We first consider an incompressible fluid to identify the separate characteristics of sound propagation and viscous diffusion in the hydrodynamic interactions. We then consider a compressible fluid to consider the effect of the order of magnitude relation of the sound propagation and viscous diffusion time scales on the temporal evolution of the hydrodynamic interactions. In addition, we examine the validity of analytical solutions within the Oseen approximation, which are often compared with experimental results.

3.2 Model

3.2.A Basic equations

We obtain solutions to describe the dynamics of particles in a Newtonian fluid. The motion of the particles is governed by Newton's and Euler's equations of motion, which can be written for the i-th particle as

$$M_i \frac{\mathrm{d}}{\mathrm{d}t} \boldsymbol{V}_i = \boldsymbol{F}_i^H + \boldsymbol{F}_i^C + \boldsymbol{F}_i^E, \qquad \frac{\mathrm{d}}{\mathrm{d}t} \boldsymbol{R}_i = \boldsymbol{V}_i, \tag{3.2}$$

$$I_i \cdot \frac{\mathrm{d}}{\mathrm{d}t}\mathbf{\Omega}_i = \mathbf{N}_i^H + \mathbf{N}_i^E, \tag{3.3}$$

where $\mathbf{R}_i$, $\mathbf{V}_i$, and $\mathbf{\Omega}_i$ are the position, the translational velocity, and the rotational velocity of the i-th particle, respectively. The particle has a mass M_i and a moment of inertia $\mathbf{I}_i$. The fluid exerts a hydrodynamic force $\mathbf{F}_i^H$ and a torque $\mathbf{N}_i^H$ on the particle, while a force $\mathbf{F}_i^C$ is exerted through direct interactions among the particles. A force $\mathbf{F}_i^E$ and torque $\mathbf{N}_i^E$ are externally applied. The hydrodynamic force and torque are evaluated from the momentum conservation between the particle and the fluid.

The fluid dynamics are governed by the following hydrodynamic equations:

$$\frac{\partial \rho}{\partial t} + \mathbf{\nabla} \cdot (\rho \mathbf{v}) = 0, \tag{3.4}$$

$$\frac{\partial \rho \mathbf{v}}{\partial t} + \mathbf{\nabla} \cdot (\rho \mathbf{v}\mathbf{v}) = \mathbf{\nabla} \cdot \boldsymbol{\sigma} + \mathbf{f}^R, \tag{3.5}$$

where $\rho(\mathbf{r}, t)$ and $\mathbf{v}(\mathbf{r}, t)$ are the mass density and velocity fields, respectively, of the fluid. The stress tensor is given by

$$\boldsymbol{\sigma} = -p\mathbf{I} + \eta[\mathbf{\nabla}\mathbf{v} + (\mathbf{\nabla}\mathbf{v})^T] + \left(\eta_v - \frac{2}{3}\eta\right)(\mathbf{\nabla} \cdot \mathbf{v})\mathbf{I}, \tag{3.6}$$

where $p(\mathbf{r}, t)$ is the pressure, η is the shear viscosity, and η_v is the bulk viscosity. A body force $\mathbf{f}^R(\mathbf{r}, t)$ is added to satisfy particle rigidity. We also assume a barotropic fluid described by $p = p(\rho)$ with a constant speed of sound c such that

$$\frac{\mathrm{d}p}{\mathrm{d}\rho} = c^2. \tag{3.7}$$

Equations (3.4)-(3.7) are closed for the variables ρ, $\mathbf{v}$, and p, without consideration of energy conservation.

We use SPM to perform direct numerical simulations. In this method, the boundaries between particle and fluid are modeled by a continuous interface. For this purpose, a smoothed profile function $\phi(\mathbf{r}, t) \in [0, 1]$ is introduced to distinguish between the particle and fluid domains: i.e., $\phi = 1$ in the particle domain and $\phi = 0$ in the fluid domain. These two domains are smoothly connected through a thin interfacial region of thickness ξ. The body force for the particle rigidity $\mathbf{f}^R$ is expressed as $\rho\phi\mathbf{f}_p$. The detailed mathematical expressions of ϕ and $\phi\mathbf{f}_p$ have been previously given.[9]
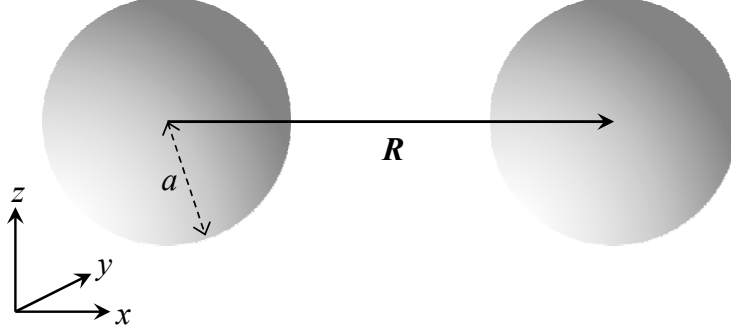
Figure 3.1: Geometry of the present model system. Two spherical particles of equal radius a are situated in a fluid with a center-to-center distance $R = |\boldsymbol{R}|$. This system is axisymmetric about the $\boldsymbol{R} = \boldsymbol{R}_2 - \boldsymbol{R}_1$ direction, such that two directions are of interest: parallel and perpendicular to the center-to-center axis of the particles. In this figure, the y and z directions are degenerate perpendicular directions.

3.2.B Linear formulation

The hydrodynamic equations can be linearized for slow flows in a dispersion. Correspondingly, the equations of motion of the particles are also linear. Most approximate theories are based on this formulation.

Here, for a N_p-particle system, we define the following column vectors to describe the equations concisely:

$$
\boldsymbol{U} = \begin{pmatrix} \boldsymbol{V}_1 \\ \vdots \\ \boldsymbol{V}_{N_p} \\ \boldsymbol{\Omega}_1 \\ \vdots \\ \boldsymbol{\Omega}_{N_p} \end{pmatrix}, \quad
\boldsymbol{H} = \begin{pmatrix} \boldsymbol{F}_1^H \\ \vdots \\ \boldsymbol{F}_{N_p}^H \\ \boldsymbol{N}_1^H \\ \vdots \\ \boldsymbol{N}_{N_p}^H \end{pmatrix}, \quad
\boldsymbol{E} = \begin{pmatrix} \boldsymbol{F}_1^E \\ \vdots \\ \boldsymbol{F}_{N_p}^E \\ \boldsymbol{N}_1^E \\ \vdots \\ \boldsymbol{N}_{N_p}^E \end{pmatrix},
$$

which are the $6N_p$-dimensional vectors. Neglecting direct particle interactions, the equations of particle motion, i.e., Eqs. (3.2) and (3.3) are summarized by

$$
\boldsymbol{M} \cdot \frac{\mathrm{d}}{\mathrm{d}t} \boldsymbol{U}(t) = \boldsymbol{H}(t) + \boldsymbol{E}(t), \tag{3.8}
$$

where the matrix $\boldsymbol{M}$ represents the direct sum of the mass tensor and the moment of inertia tensor. For spherical particles with equal radii and densities, the matrix $\boldsymbol{M}$ reduces to

$$
\boldsymbol{M} = \begin{pmatrix} M\boldsymbol{I}_{3N_p} & \boldsymbol{0} \\ \boldsymbol{0} & \frac{2}{5}Ma^2\boldsymbol{I}_{3N_p} \end{pmatrix}, \tag{3.9}
$$

where M and a are the mass and the radius, respectively, of each particle. With Fourier transforming Eq. (3.8), the corresponding equation for the Fourier components with the time factor $e^{-i\omega t}$ is

obtained by

$$-i\omega \boldsymbol{M} \cdot \hat{\boldsymbol{U}}(\omega) = \hat{\boldsymbol{H}}(\omega) + \hat{\boldsymbol{E}}(\omega). \tag{3.10}$$

The following relation holds true for the linearized hydrodynamic equations:[2]

$$\hat{\boldsymbol{U}}(\omega) = -\hat{\boldsymbol{\mu}}(\omega) \cdot \hat{\boldsymbol{H}}(\omega), \tag{3.11}$$

where $\hat{\boldsymbol{\mu}}$ is the $6N_p \times 6N_p$ mobility matrix. The mobility matrix depends on the configuration of all the particles $\{\boldsymbol{R}_i\}$, so we further assume, for simplicity, that the particles do not move significantly over the time scale considered, namely, the configuration of particles $\{\boldsymbol{R}_i\}$ is independent of time t. Substitution of Eq. (3.11) into Eq. (3.10) yields an explicit expression for the translational and rotational particle velocities:

$$\hat{\boldsymbol{U}}(\omega) = [\boldsymbol{I} - i\omega\hat{\boldsymbol{\mu}}(\omega) \cdot \boldsymbol{M}]^{-1} \cdot \hat{\boldsymbol{\mu}}(\omega) \cdot \hat{\boldsymbol{E}}(\omega). \tag{3.12}$$

Therefore, for an externally applied force and torque, the dynamics of particles in a fluid can be described by the mobility matrix.

The components of the mobility matrix are given by

$$\hat{\boldsymbol{\mu}}(\omega) = \begin{pmatrix} \hat{\boldsymbol{\mu}}^{\mathrm{tt}}(\omega) & \hat{\boldsymbol{\mu}}^{\mathrm{tr}}(\omega) \\ \hat{\boldsymbol{\mu}}^{\mathrm{rt}}(\omega) & \hat{\boldsymbol{\mu}}^{\mathrm{rr}}(\omega) \end{pmatrix}, \tag{3.13}$$

where $\hat{\boldsymbol{\mu}}^{\alpha\beta}$ is the $3N_p \times 3N_p$ matrix, which is composed of the mobility tensors $\hat{\boldsymbol{\mu}}_{ij}^{\alpha\beta}$ for two particles i and j. The mobility tensors describe the mutual coupling of the translational and rotational motion between particles and the superscript represents the mode of the motion: 't' for translation and 'r' for rotation. The mobility matrix is symmetric as a consequence of the Lorentz reciprocal theorem, such that the following relations are satisfied:[12]

$$\hat{\boldsymbol{\mu}}^{\mathrm{tt}} = (\hat{\boldsymbol{\mu}}^{\mathrm{tt}})^T, \quad \hat{\boldsymbol{\mu}}^{\mathrm{rr}} = (\hat{\boldsymbol{\mu}}^{\mathrm{rr}})^T, \quad \hat{\boldsymbol{\mu}}^{\mathrm{tr}} = (\hat{\boldsymbol{\mu}}^{\mathrm{rt}})^T. \tag{3.14}$$

Now, we consider a system of two identical spherical particles in a fluid. The configuration of the particles is described in Fig. 3.1. Numbers are assigned to the particles: 1 for the particle on the left and 2 for the particle on the right. We define a vector $\boldsymbol{R} = \boldsymbol{R}_2 - \boldsymbol{R}_1$ to describe the geometry of this system. The particle center-to-center distance is denoted by $R = |\boldsymbol{R}|$. The unit vector along the line of centers is described by $\hat{\boldsymbol{R}} = \boldsymbol{R}/R$. Due to axisymmetry about the $\hat{\boldsymbol{R}}$ axis, each mobility tensor is described by at most two scalar functions:[13,14]

$$\hat{\boldsymbol{\mu}}_{ij}^{\mathrm{tt}}(\boldsymbol{R}, \omega) = \hat{\mu}_{ij}^{\mathrm{tt}\|}(R, \omega)\hat{\boldsymbol{R}}\hat{\boldsymbol{R}} + \hat{\mu}_{ij}^{\mathrm{tt}\perp}(R, \omega)(\boldsymbol{I} - \hat{\boldsymbol{R}}\hat{\boldsymbol{R}}), \tag{3.15a}$$

$$\hat{\boldsymbol{\mu}}_{ij}^{\mathrm{rr}}(\boldsymbol{R},\omega) = \hat{\mu}_{ij}^{\mathrm{rr}\|}(R,\omega)\hat{\boldsymbol{R}}\hat{\boldsymbol{R}} + \hat{\mu}_{ij}^{\mathrm{rr}\perp}(R,\omega)(\boldsymbol{I} - \hat{\boldsymbol{R}}\hat{\boldsymbol{R}}), \tag{3.15b}$$

$$\hat{\boldsymbol{\mu}}_{ij}^{\mathrm{tr}}(\boldsymbol{R},\omega) = \hat{\mu}_{ij}^{\mathrm{tr}\perp}(R,\omega)\hat{\boldsymbol{R}} \times \boldsymbol{I}. \tag{3.15c}$$

The superscripts $\|$ and $\perp$ denote the directions of motion parallel and perpendicular to the symmetry axis, respectively. In the direction parallel to the symmetry axis, the translational and rotational motions are decoupled as indicated by Eq. (3.15c). Interchanging the particle numbers 1 and 2 corresponds to inverting the direction of $\hat{\boldsymbol{R}}$, which causes sign inversion for the translation-rotation cross-mobility tensor $\hat{\boldsymbol{\mu}}_{ij}^{\mathrm{tr}}$ without changing sign of the other cross-mobility tensors $\hat{\boldsymbol{\mu}}_{ij}^{\mathrm{tt}}$ and $\hat{\boldsymbol{\mu}}_{ij}^{\mathrm{rr}}$. The mobility tensors Eqs. (3.15) within the Oseen approximation are described in the Appendix.

3.2.C Temporal evolution of the flow field

We first consider a particle dispersion with an incompressible fluid solvent. Incompressibility corresponds to an infinite speed of sound in the fluid, such that the solenoidal condition is imposed on the fluid velocity field from Eqs. (3.4) and (3.7) as

$$\boldsymbol{\nabla} \cdot \boldsymbol{v} = 0. \tag{3.16}$$

The velocity field can be decomposed into two contributions as

$$\boldsymbol{v} = \boldsymbol{w} - \boldsymbol{\nabla}\varphi. \tag{3.17}$$

The vector field $\boldsymbol{w}(\boldsymbol{r},t)$ is the juxtaposition of the velocity fields in the fluid and particle domains, so that the fluid-particle impermeability boundary condition, or the continuity of the normal velocity on the boundary, is not satisfied. An irrotational flow field, described by the scalar potential $\varphi(\boldsymbol{r},t)$, is added in order that the velocity field $\boldsymbol{v}$ satisfies the boundary condition. Due to the solenoidal condition on the velocity field $\boldsymbol{v}$, the scalar potential φ obeys the Poisson equation:

$$\boldsymbol{\nabla}^2\varphi = \boldsymbol{\nabla} \cdot \boldsymbol{w}. \tag{3.18}$$

On the right-hand side, $\boldsymbol{\nabla} \cdot \boldsymbol{w}$ is zero except at the fluid-particle boundary, at which singularities exist. From Eq. (3.18), the scalar potential is given by[15]

$$\varphi(\boldsymbol{r},t) = -\frac{1}{4\pi}\int \mathrm{d}\boldsymbol{r}' \frac{(\boldsymbol{r} - \boldsymbol{r}')}{|\boldsymbol{r} - \boldsymbol{r}'|^3} \cdot \boldsymbol{w}(\boldsymbol{r}',t). \tag{3.19}$$

Now we consider an isolated single particle, due to axisymmetry, the scalar potential and the corresponding velocity field can be simply described as

$$\varphi(\boldsymbol{r},t) = \frac{\boldsymbol{Q}(t) \cdot \boldsymbol{r}}{r^3}, \tag{3.20}$$

32

$$-\boldsymbol{\nabla}\varphi(\boldsymbol{r},t) = \frac{\boldsymbol{Q}(t)\cdot(3\hat{\boldsymbol{r}}\hat{\boldsymbol{r}} - \boldsymbol{I})}{r^3}, \tag{3.21}$$

where $\hat{\boldsymbol{r}} = \boldsymbol{r}/r$ is a unit vector in the radial direction. The velocity field of Eq. (3.21) represents a doublet flow, which corresponds to the electric field generated by an electric dipole. The vector $\boldsymbol{Q}(t)$ is parallel to the particle velocity and depends on time in a reflection of the particle motion relative to the fluid. The analytical form of $\boldsymbol{Q}(t)$ has been derived previously,[16] and the strength $Q(t) = |\boldsymbol{Q}(t)|$ is time-independent for a neutrally buoyant particle. The doublet flow is generated instantaneously to satisfy the solenoidal condition, thus, the doublet flow is interpreted to expand at the infinite speed of sound.

The vector field $\boldsymbol{w}$ represents the shear flow due to viscous diffusion. For sufficiently slow fluid flow, the hydrodynamic equations can be linearized as follows:

$$\rho_0 \frac{\partial \boldsymbol{v}}{\partial t} = -\boldsymbol{\nabla}p + \eta\boldsymbol{\nabla}^2\boldsymbol{v} + \boldsymbol{f}^R. \tag{3.22}$$

Under the incompressibility condition, the pressure gradient imposes fluid-particle impermeability on the time-derivative of the velocity field, so that the pressure is related to the scalar potential as

$$p = \rho_0 \frac{\partial \varphi}{\partial t}. \tag{3.23}$$

Therefore, the temporal evolution of the vector field $\boldsymbol{w}$ is given by

$$\rho_0 \frac{\partial \boldsymbol{w}}{\partial t} = \eta(\boldsymbol{\nabla}^2\boldsymbol{w} - \boldsymbol{\nabla}\boldsymbol{\nabla}\cdot\boldsymbol{w}) + \boldsymbol{f}^R. \tag{3.24}$$

Modifying the diffusion term on the right-hand side to be solenoidal, results in the doublet flow being gradually offset by the diffusion of the vector field $\boldsymbol{w}$.

In short, the exertion of an impulsive force on a particle in an incompressible fluid instantaneously generates a doublet flow. The shear flow then spreads out diffusely, cancelling out the doublet flow. This picture will be validated in one of the following numerical simulation results.

For a compressible fluid, a second contribution is added to Eq. (3.17):

$$\boldsymbol{v} = \boldsymbol{w} - \boldsymbol{\nabla}\psi - \boldsymbol{\nabla}\varphi, \tag{3.25}$$

where the scalar potential $\psi(\boldsymbol{r},t)$ corresponds to the bulk compression flow. Here, we assume that the dynamics of fluid can be described by the linearized hydrodynamic equations:

$$\frac{\partial p}{\partial t} = -\rho_0 c^2 \boldsymbol{\nabla}\cdot\boldsymbol{v}, \tag{3.26}$$

$$\rho_0 \frac{\partial \boldsymbol{v}}{\partial t} = \eta \boldsymbol{\nabla}^2 \boldsymbol{v} + \left(\frac{1}{3}\eta + \eta_v \right) \boldsymbol{\nabla} \boldsymbol{\nabla} \cdot \boldsymbol{v} - \boldsymbol{\nabla} p + \boldsymbol{f}^R. \tag{3.27}$$

The time evolution equation of the total scalar potential $\varphi' = \varphi + \psi$ is derived from the equations above as

$$\boldsymbol{\nabla}^2 \varphi' - \frac{1}{c^2}\frac{\partial^2 \varphi'}{\partial t^2} + \frac{\eta_l}{\rho_0 c^2}\boldsymbol{\nabla}^2 \frac{\partial \varphi'}{\partial t} = \left(1 + \frac{\eta_l}{\rho_0 c^2}\boldsymbol{\nabla}^2 \frac{\partial}{\partial t} \right)(\boldsymbol{\nabla} \cdot \boldsymbol{w}), \tag{3.28}$$

where $\eta_l = (4/3)\eta + \eta_v$ denotes the longitudinal viscosity. This is a damped wave equation, where the source is given on the right-hand side of the equation. Therefore, a potential flow propagates at a finite speed of sound in a compressible fluid. In the long-time limit, Eq. (3.28) reduces to the Poisson equation for an incompressible fluid, as given by Eq. (3.18), and the potential flow reduces to an instantaneous doublet flow.

3.3 Numerical Results

Numerical simulations are performed for a three-dimensional box with periodic boundary conditions. The space is divided into meshes of length Δ, which is a unit length. The units of the other physical quantities are defined by combining $\eta = 1$ and $\rho_0 = 1$ with Δ, where ρ_0 is the fluid mass density at equilibrium. The system size is $L_x \times L_y \times L_z = 256 \times 256 \times 256$. The other parameters are set to $a = 4$, $\xi = 2$, $\rho_p = 1$, $\eta_v = 0$, and $h = 0.05$, where ρ_p is the particle mass density and h is the time increment of a single simulation step.

We consider a system in which two identical spherical particles in a fluid, whose geometry is described in Fig 3.1. Both particles have the same density and radius, namely the same mass and moment of inertia. We investigate the time-dependence of the velocity for particle 1 following the exertion of an impulsive force at the center of particle 2, with changing the center-to-center distance between particles given by $R^* = R/a$. This cross-relaxation function is a manifestation of the temporal evolution of the hydrodynamic interactions between particles 1 and 2. The impulsive force is assumed to be sufficiently small such that the Reynolds and Mach numbers of the flow are sufficiently low. We set the impulsive force to produce an initial particle Reynolds number of $\mathrm{Re}_p = 10^{-3}$. In addition, because the particle displacement before stopping, scaled by the particle radius a, is comparable to $(\rho_p/\rho_0)\mathrm{Re}_p$, the displacement of particles is negligible in the present simulations. Therefore, because particle collisions do not occur, the direct interactions between particles, including overlap repulsion forces, are not considered.

34

The cross-relaxation tensor is introduced as the normalized change in velocity of particle 1:

$$\boldsymbol{V}_1(\boldsymbol{R}_1, t; \boldsymbol{R}_2) = \frac{\boldsymbol{P}_2}{M} \cdot \boldsymbol{\gamma}_{12}(\boldsymbol{R}, t), \tag{3.29}$$

$$\boldsymbol{\gamma}_{12}(\boldsymbol{R}, t) = \gamma_{12}^{\parallel}(R, t)\hat{\boldsymbol{R}}\hat{\boldsymbol{R}} + \gamma_{12}^{\perp}(R, t)(\boldsymbol{I} - \hat{\boldsymbol{R}}\hat{\boldsymbol{R}}), \tag{3.30}$$

where $\boldsymbol{P}_2$ is the impulsive force exerted on particle 2 at $t = 0$. Due to the previously mentioned axisymmetry, the cross-relaxation tensor is characterized by only two directions of motion, which are parallel and perpendicular to the center-to-center vector $\boldsymbol{R}$. Then, the motions in both directions are decoupled. From the fluctuation-dissipation theorem, the cross-relaxation tensor is equivalent to the velocity cross-correlation function of the fluctuating system:

$$\boldsymbol{\gamma}_{12}(\boldsymbol{R}, t) = \frac{M}{k_B T} \langle \boldsymbol{V}_1(\boldsymbol{0}, 0)\boldsymbol{V}_2(\boldsymbol{R}, t) \rangle, \tag{3.31}$$

where k_B is the Boltzmann constant and T is the thermodynamic temperature. We examine both the parallel correlation $\gamma_{12}^{\parallel}$ and the perpendicular correlation $\gamma_{12}^{\perp}$ by adjusting the direction of the impulsive force $\boldsymbol{P}_2$. As predicted by the formulation in the preceding section, for motion perpendicular to the axis, the translation-rotation coupling in the particle motion is also observed. However, because the influence of sound propagation on the rotational motion is expected to be small, we will focus entirely on the translation-translation coupling. We also compare the simulated results with approximate solutions, where the analytical solution for an isolated single particle for the self-mobilities and the Oseen approximation for the cross-mobilities are applied (see the Appendix).

3.3.A   Incompressible fluid

First, we investigate the temporal evolution of hydrodynamic interactions in an incompressible fluid. The dynamics of the incompressible fluid is governed by the hydrodynamic equations composed of Eqs. (3.5), (3.6), and (3.16). The center-to-center distance between particles takes values of $R^* = 3$, 4, and 7. The simulation results for the velocity cross-relaxation functions are shown in Fig. 3.2. While the parallel correlation $\gamma_{12}^{\parallel}(t)$ is positive at all times, The perpendicular correlation $\gamma_{12}^{\perp}(t)$ is initially negative and subsequently becomes positive. Comparable results have been reported in experimental studies,[3–5] where the difference between the parallel and perpendicular correlations has been attributed to the flow field around the particle.[4,7] We discuss the time-dependence of the velocity cross-relaxation functions in more detail below.
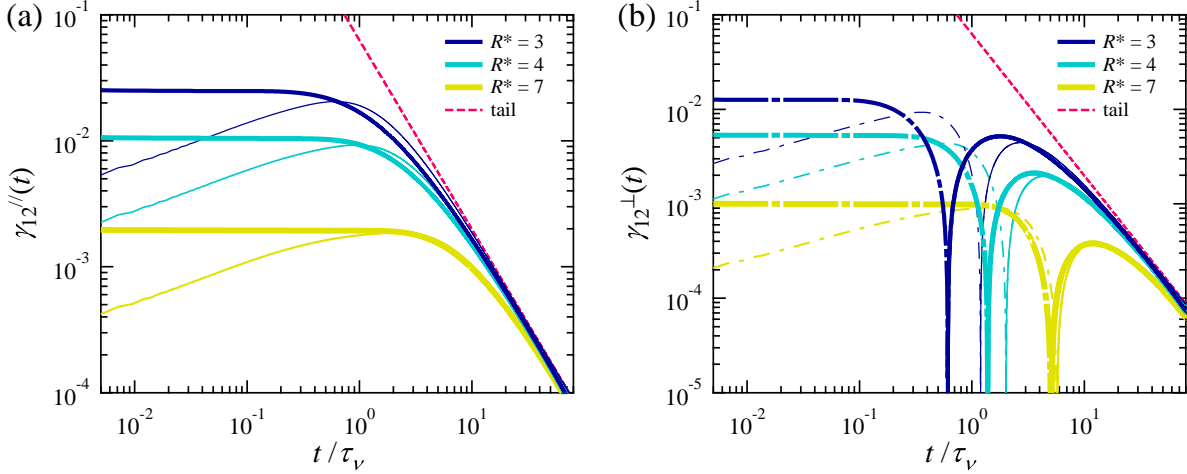
Figure 3.2: Velocity cross-relaxation function in an incompressible fluid in (a) parallel and (b) perpendicular directions relative to the symmetry axis of the particles. The distance between the two particles are $R^* = 3$, 4, and 7. Simulation results are described by bold solid lines (positive values) and dashed-dotted lines (negative values). Solutions within the Oseen approximation are represented by thin solid lines (positive values) and dashed-dotted lines (negative values). The broken line represents the long-time tail with the algebraic power law decay $Bt^{-3/2}$, as given by Eq. (3.32).

The temporal evolution of the flow field has been explained in the previous section. Here, the velocity fields generated by the impulsive force exerted on a single particle are shown in Fig. 3.3. These simulation results are obtained for a single particle system with size $L_x \times L_y \times L_z = 128 \times 128 \times 128$. At early times $t/\tau_\nu = 2.5 \times 10^{-2}$, the doublet flow is dominant. The doublet flow is characterized by loop streamlines flared in the direction perpendicular to the particle motion, where backflow is observed as described by Eq. (3.20). As discussed in the previous section, the doublet flow appears instantaneously, which is interpreted as the propagation of an infinite-speed sound wave. On the other hand, the shear flow due to viscous diffusion, whose strength is given by the vorticity $\nabla \times v$, is only observed in the vicinity of the particle. Over a time $t/\tau_\nu = 1.2$, the shear flow has diffused over a large range following Eq. (3.24); therefore, there is a spreading fluid region flowing in the same direction as the particle motion, while the loop streamlines get away from the particle.

The velocity cross-relaxation function is related to the temporal evolution of the flow field around particle 2. The doublet flow propagated by sound waves produces an instantaneous velocity correlation between the particles. The doublet flow direction shown in Fig. 3.3 produces the positive parallel correlation and the negative perpendicular correlation. Little change in the cross-relaxation
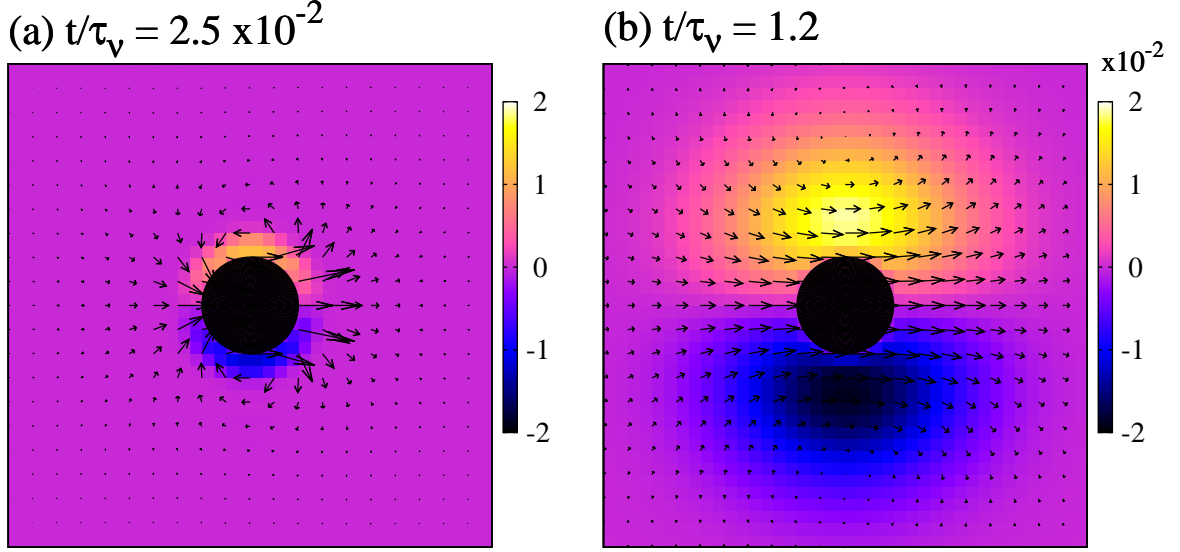
Figure 3.3: Temporal evolution of the velocity field around an isolated single particle due to an impulsive force exerted on the particle in an incompressible fluid. The cross-sections parallel to the impulsive force direction including the particle center are shown. The impulsive force is exerted at time $t = 0$ and the simulation results are given at (a) $t/\tau_\nu = 2.5 \times 10^{-2}$ and (b) $t/\tau_\nu = 1.2$. The direction of the impulsive force is to the right in the pictures and the particle is represented by a black circle. The vorticity of the velocity field $\nabla \times \boldsymbol{v}$ is described by a color scale, going from negative (darker) to positive (lighter) vorticity. The vorticity is normalized by τ_ν/Re_p.

functions occurs in the early stages, reflecting the time-independence of the strength of the doublet flow due to the neutrally buoyant particle.[16]

The reduction in the parallel correlation and the sign inversion of the perpendicular correlation occur at about the same time, which depends on the inter-particle distance R^*. Because shear flow by viscous diffusion can cause such changes in the cross-relaxation functions, we estimate the time scale on which the shear flow generated by the particle 2 arrives at particle 1 by the viscous diffusion time scale over the length L: $\tau_\nu^* = L^2/\nu$. In this case, the characteristic length is the distance between the particle surfaces, $L = R - 2a$; thus, for $R^* = 3$, 4, and 7, the viscous diffusion time scales are $\tau_\nu^*/\tau_\nu = (R^* - 2)^2 = 1$, 4, and 25, respectively. The time for the parallel correlation to begin decreasing and for the perpendicular correlation to invert the sign roughly corresponds to τ_ν^* in each case.

In an incompressible fluid, hydrodynamic interactions are instantly propagated at the infinite speed of sound and subsequently transmitted by viscous diffusion in a time scale τ_ν^*. The temporal evolution of the flow fields around two particles separated by $R^* = 7$ is shown in Fig. 3.4. At early times in the flow, $t/\tau_\nu = 6.25 \times 10^{-1}$ so that the shear flow does not arrive at particle 1, whose dynamics are governed by the doublet flow. Later, at $t/\tau_\nu = 12.5$, the shear flow diffuses
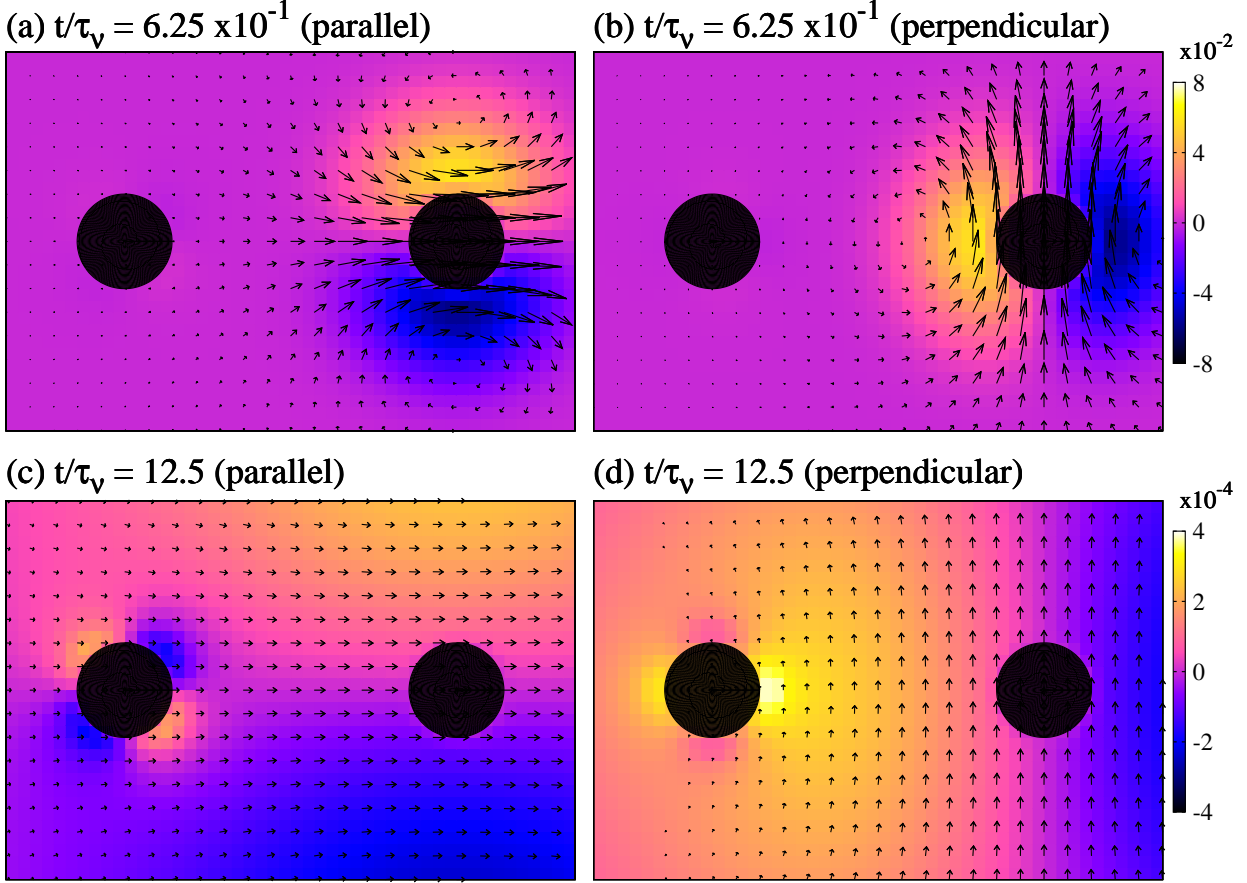
37

Figure 3.4: Temporal evolution of the velocity field around the particles. The cross-sections including the center-to-center axis between particles are shown. The center-to-center distance between two particles is $R^* = 7$. The impulsive force is exerted at time $t = 0$ on the particle on the right and the simulation results are presented at (a,b) $t/\tau_\nu = 6.25 \times 10^{-1}$ and (c,d) $t/\tau_\nu = 12.5$. The direction of the impulsive force is (a,c) to the right and (b,d) upwards. The particles are represented by black circles. The vorticity of the velocity field $\nabla \times \boldsymbol{v}$ is described by a color scale, going from negative (darker) to positive (lighter) vorticity. The vorticity is normalized by τ_ν/Re_p.

over time to arrive at particle 1 and the motion of particle 1 is governed by the shear flow. Here, the stresslet flow field is observed in the vicinity of particle 1. This flow is generated to maintain particle rigidity against deformation in a shear flow. In the perpendicular correlation, the rotational motion of particle 1 is also observed.

In the final stages of the flow, the momentum of particle 2 has completely diffused away, so that the particles and the fluid move collectively. These dynamics are manifested in a long-time tail with a power law decay $t^{-3/2}$ of the cross-relaxation functions shown in Fig. 3.2, which are given by[17]

$$\gamma_{12}^{\parallel,\perp}(t) = \frac{1}{9\sqrt{\pi}} \frac{\rho_p}{\rho_0} \left(\frac{\tau_\nu}{t} \right)^{3/2} \quad \text{as} \quad t \to \infty. \tag{3.32}$$

Discrepancies between the simulation results and the Oseen approximation are observed, espe-

cially at $t/\tau_\nu \lesssim 3$, as shown in Fig. 3.2. The approximate cross-relaxation functions clearly change with time in the early stages and the time at which the effect of the shear flow becomes apparent is later than in the simulation results. Particles are assumed to be points in the Oseen approximation; therefore, this approximation implies that the particle separation is much larger than the particle radius as $R^* = R/a \gg 1$ and that the time scale of observation is much longer than that of viscous diffusion over the length of the particle radius as $t/\tau_\nu = t\nu/a^2 \gg 1$. Neglecting the particle size results in a larger characteristic length $L = R$ and a longer diffusion time scale $\tau_\nu^*/\tau_\nu = R^{*2}$. Consequently, the Oseen approximation can only be accurately applied at long times and large particle separations. The simulation results shown in Fig. 3.2 confirm that the validity of the Oseen approximation increases with increasing inter-particle distance R^*. In previous experimental studies, measurements were conducted over the range for which the Oseen approximation is valid, i.e., $R^* \gtrsim 5$ and measuring frequencies corresponding to $t/\tau_\nu \gtrsim 30$: consequently, the experimental results showed good agreement with the Oseen approximation.[3,4]

3.3.B   Compressible fluid

Next, we consider a compressible fluid in which sound propagates at a finite speed. The velocity cross-relaxation functions for inter-particle distances $R^* = 3$ and 7 are shown in Figs. 3.5 and 3.6, respectively. Due to the periodic boundary conditions imposed on the simulation box, a sound pulse generated by the particle motion can affect the simulation results after the sound pulse arrives at the end of the simulation box. The oscillatory structure of the cross-relaxation functions, especially at $\varepsilon = 0.1$, is one of the striking artifacts of the periodic boundary conditions.

The velocity cross-relaxation functions are zero in the early stages and then suddenly change to non-zero values. Because this time lag increases with the inter-particle separation, this is likely to be due to the sound propagation from particle 2 to particle 1. As with the diffusion of shear flow, we estimate the time scale for sound propagation over a characteristic length $L = R - 2a$ as $\tau_c^* = L/c$. For $R^* = 3$ and 7, the sound propagation time scales are $\tau_c^*/\tau_\nu = (R^* - 2)\varepsilon = \varepsilon$ and 5ε, respectively. The results shown in Figs. 3.5 and 3.6 confirm the correspondence between the time scale of sound propagation and the peak of the cross-relaxation functions. The peak in the cross-relaxation function broadens as sound propagation is dissipated by the longitudinal viscosity according to Eq. (3.28). The velocity fields around particles separated by $R^* = 7$ at $t/\tau_\nu = 6.25 \times 10^{-1}$ are shown in Fig. 3.7. The expanding doublet flow with a strength given by
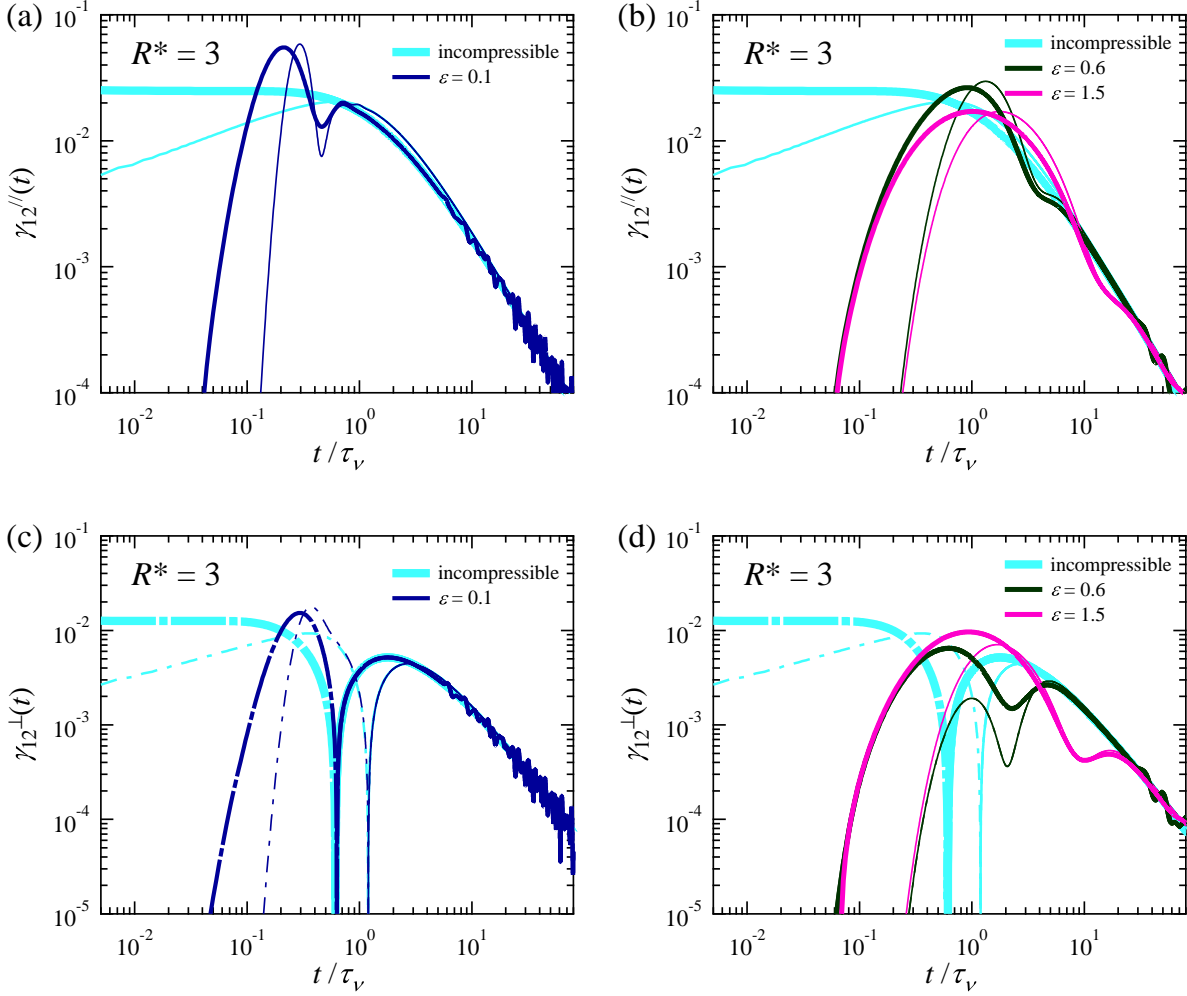
Figure 3.5: Velocity cross-relaxation function in a compressible fluid in (a, b) parallel and (c, d) perpendicular directions to the symmetry axis. The center-to-center distance between two particles is $R^* = 3$. The compressibility factor takes values of $\varepsilon = 0.1$, 0.6, and 1.5. Simulation results are described by bold solid lines (positive values) and dashed-dotted lines (negative values). Solutions within the Oseen approximation are represented by thin solid lines (positive values) and dashed-dotted lines (negative values).

the divergence of the velocity field $\boldsymbol{\nabla} \cdot \boldsymbol{v}$ are observed. For a small compressibility factor $\varepsilon = 0.1$, the doublet flow has just arrived at particle 1. This situation corresponds to a peak in the cross-relaxation functions shown in Fig. 3.6(a,c). On the other hand, for a large compressibility factor $\varepsilon = 0.6$, the doublet flow has not yet arrived at particle 1 and the cross-relaxation functions are correspondingly zero.

When the fluid compressibility is as small as $\varepsilon = 0.1$, the velocity cross-relaxation functions superimpose onto those for the incompressible fluid after a time τ_c^*. This behavior only describes hydrodynamic interactions by sound propagation before viscous diffusion effects come into play. On
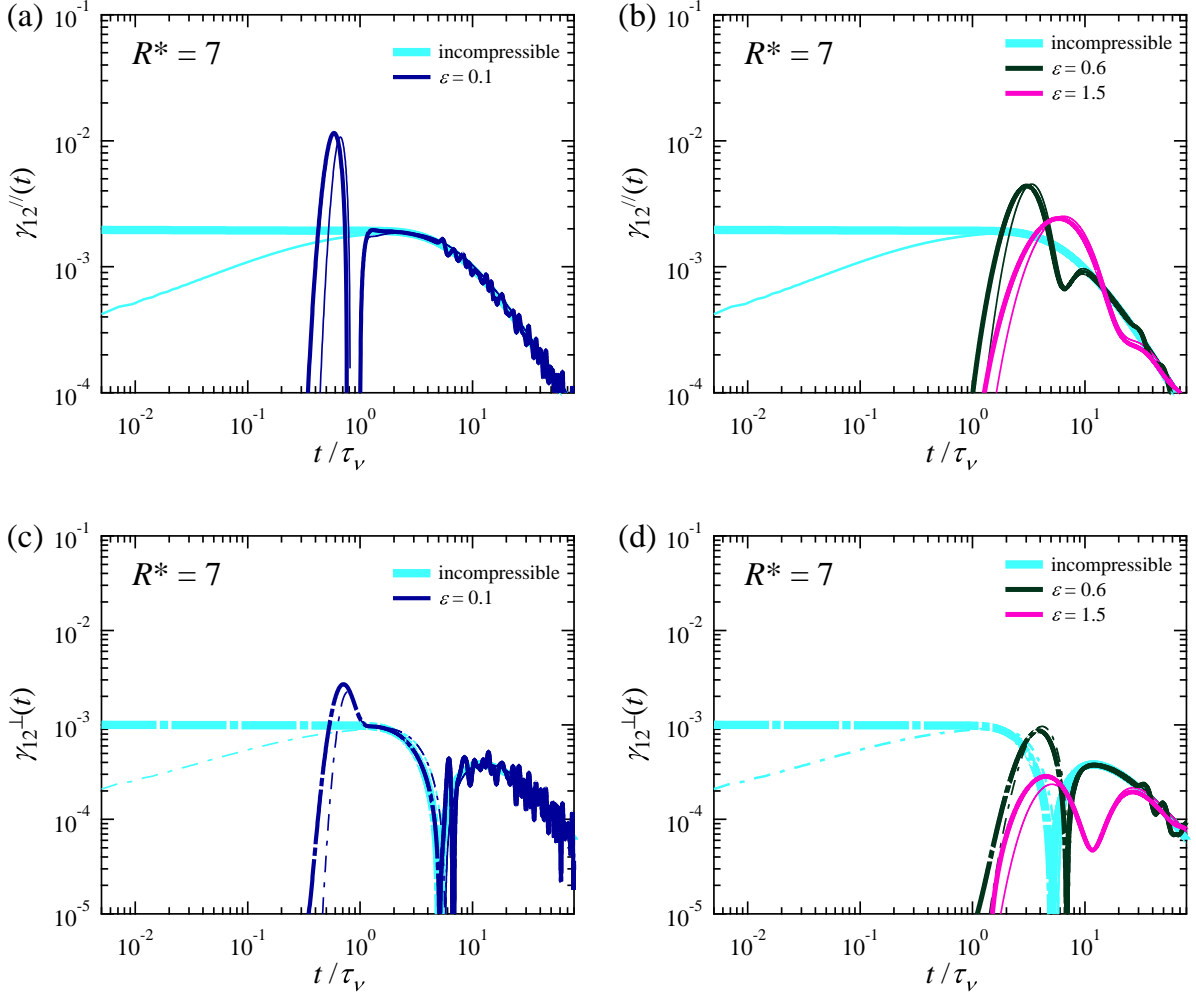
Figure 3.6: Velocity cross-relaxation function in a compressible fluid in (a, b) parallel and (c, d) perpendicular directions to the symmetry axis. The center-to-center distance between two particles is $R^* = 7$. The compressibility factor takes values of $\varepsilon = 0.1$, 0.6, and 1.5. Simulation results are described by bold solid lines (positive values) and dashed-dotted lines (negative values). Solutions within the Oseen approximation are represented by thin solid lines (positive values) and dashed-dotted lines (negative values).

the other hand, for a large compressibility $\varepsilon = 1.5$, the behavior of the cross-relaxation functions are considerably different, except for the hydrodynamic long-time tail: in particular, there is no negative perpendicular correlation. For a fluid with medium compressibility such as $\varepsilon = 0.6$, the negative perpendicular correlation is observed only for inter-particle separations as large as $R^* = 7$. As sound propagation and viscous diffusion generate negative and positive perpendicular correlations, respectively, the balance of the two time scales τ_ν^* and τ_c^* is expected to characterize the behavior of the cross-relaxation function. Therefore, we define the interactive compressibility
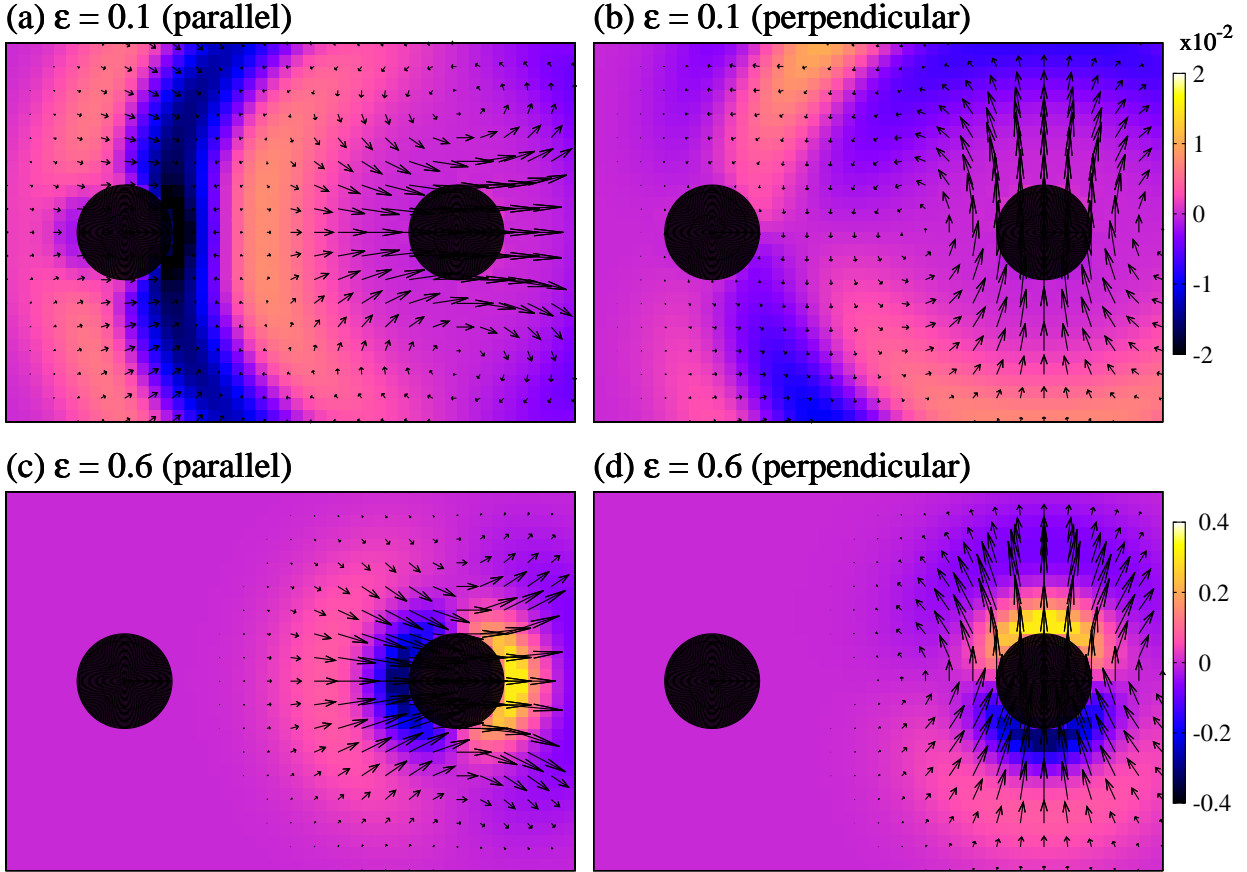
Figure 3.7: Velocity field around particles in a compressible fluid. Simulation results at $t/\tau_\nu = 6.25 \times 10^{-1}$ for compressibility factors with values (a,b) $\varepsilon = 0.1$ and (c,d) $\varepsilon = 0.6$. The divergence of the velocity field $\boldsymbol{\nabla} \cdot \boldsymbol{v}$ is described by a color scale, going from negative (darker) to positive (lighter) divergence. The value of divergence is normalized by τ_ν/Re_p.

factor using a characteristic length $L = R - 2a$ as

$$\varepsilon^* = \frac{\tau_c^*}{\tau_\nu^*} = \frac{\varepsilon}{R^* - 2}. \tag{3.33}$$

As the inter-particle distance increases, the two time scales separate to reduce the interactive compressibility factor. In the present simulations, the interactive compressibility factors for $R^* = 3$ and 7 are $\varepsilon^* = \varepsilon$ and 0.2ε, respectively. When the interactive compressibility factor is small, hydrodynamic interactions propagating at the speed of sound arrive first at the other particle in about a time τ_c^*, followed by those propagating by viscous diffusion arriving in about a time τ_ν^*. The temporal evolution is qualitatively the same as in an incompressible fluid, except for the time lag due to sound propagation at a finite speed. This situation applies to the results where a negative perpendicular correlation is observed. On the other hand, if the interactive compressibility factor is sufficiently large, the order of arrival of sound propagation and viscous diffusion should be reversed. In this situation, the perpendicular correlation is positive from the start due to viscous diffusion
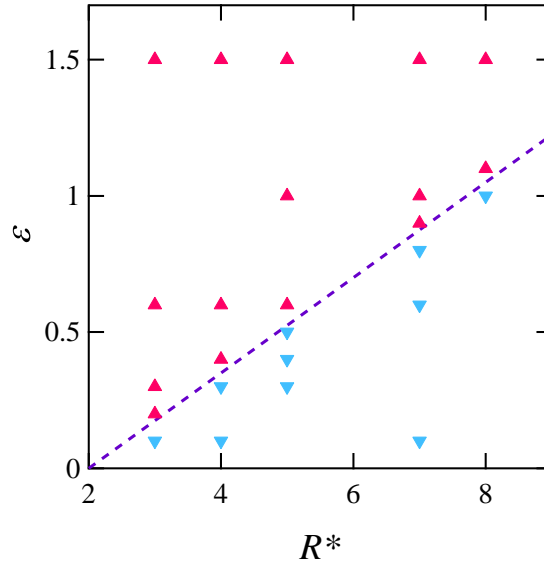
Figure 3.8: Classification of calculated cross-relaxation functions for various center-to-center distances of particles and compressibility factors. The cross-relaxation functions are classified according to the sign of the perpendicular correlation in the first stage: negative and positive are represented by downward and upward triangles, respectively. The broken line represents Eq. (3.33) with $\varepsilon^* = 0.175$.

and the effect of sound propagation on the hydrodynamic interactions produces a local minimum or temporary negative values in the cross-correlation function.

In Fig. 3.8, the velocity cross-relaxation functions for various particles center-to-center distances R^* and compressibility factors ε are classified according to the sign of the perpendicular correlation in the first stage. We can find that the perpendicular correlation is positive from the start when $\varepsilon^* \geq 0.175$ is satisfied. In this condition, the hydrodynamic interactions are propagated by viscous diffusion ahead of sound propagation.

In a compressible fluid, because there is a finite sound propagation time scale as well as a viscous diffusion time scale, the time condition for the validity of the Oseen approximation is given by $t \gg \max(\tau_\nu, \tau_c)$. As with the diffusion of shear flow, sound propagation from particle 2 to particle 1 is delayed within the Oseen approximation as shown in Figs. 3.5 and 3.6. This is because the sound propagation time scale is increased within this approximation so that $\tau_c^*/\tau_\nu = R^*\varepsilon$. Thus, the discrepancies with the simulation results can be fairly well-resolved by increasing the particle separation.

3.4 Conclusion

In the present study, we investigated the temporal evolution of hydrodynamic interactions for a system of two particles, using SPM to perform direct numerical simulations. Fluid compressibility was considered in examining temporal evolution by sound propagation. Hydrodynamic interactions were estimated by the velocity cross-relaxation functions, which are equivalent to the velocity cross-correlation functions in a fluctuating system.

In an incompressible fluid, hydrodynamic interactions were observed to propagate instantaneously at the infinite speed of sound, along with subsequent temporal evolution by viscous diffusion. Theoretical analysis showed that a doublet flow and shear flow are generated by sound propagation and viscous diffusion, respectively. Because the cross-relaxation function reflects the characteristics of each flow field, sound propagation and viscous diffusion are associated with negative and positive perpendicular correlations between the partice velocities, respectively. Therefore, the time at which the behavior of the cross-relaxation function changes is related to the time scale of viscous diffusion over the particle separation τ_ν^*, which is only the time scale characterizing the temporal evolution of hydrodynamic interactions in an incompressible fluid.

In a compressible fluid, sound propagates between particles in a finite time, which scales as τ_c^*. The effect of the order of magnitude relation between the two time scales τ_ν^* and τ_c^* on the cross-relaxation function was observed; an interactive compressibility factor ε^* was defined as the ratio of the two time scales given by Eq. (3.33). In our simulation results, the reversal of the order of arrival of sound propagation and viscous diffusion at the other particle was observed at $\varepsilon^* \geq 0.175$, for which the perpendicular correlation is positive from the start. In this case, the hydrodynamic interactions were largely governed by viscous diffusion.

The temporal evolution of hydrodynamic interactions does not qualitatively change from that for an incompressible fluid, as long as the interactive compressibility factor is small. Only when the interactive compressibility factor is sufficiently large can differences in the temporal evolution of hydrodynamic interactions be expected. As such a situation can be realized in a highly viscous fluid, experimental validation of the results presented here is desirable.

Appendix: Mobility Matrix in the Oseen Approximation

Hydrodynamic interactions among particles in slow flows are described by the mobility matrix discussed in §2.2. However, there is no known closed-form solution even for a two-particle system. In this section, we introduce an approximate analytical form for the mobility tensors.

For slow flows, the hydrodynamic equations can be linearized as given by Eqs. (3.26) and (3.27), and the corresponding equations for the Fourier components, with the time factor $e^{-i\omega t}$, are obtained as

$$-i\omega \hat{p}_\omega + \rho_0 c^2 \boldsymbol{\nabla} \cdot \hat{\boldsymbol{v}}_\omega = 0, \tag{3.34}$$

$$-i\omega \hat{\boldsymbol{v}}_\omega = \eta \boldsymbol{\nabla}^2 \hat{\boldsymbol{v}}_\omega + \left(\frac{1}{3}\eta + \eta_v\right) \boldsymbol{\nabla}\boldsymbol{\nabla} \cdot \hat{\boldsymbol{v}}_\omega - \boldsymbol{\nabla}\hat{p}_\omega + \hat{\boldsymbol{f}}_\omega^R. \tag{3.35}$$

The fluid velocity field generated by the body force $\boldsymbol{f}^R$ is expressed as

$$\hat{\boldsymbol{v}}_\omega(\boldsymbol{r}) = \int \mathrm{d}\boldsymbol{r}' \hat{\boldsymbol{G}}(\boldsymbol{r} - \boldsymbol{r}', \omega) \cdot \hat{\boldsymbol{f}}_\omega^R(\boldsymbol{r}'), \tag{3.36}$$

where the Green's function is given by[18,19]

$$\hat{\boldsymbol{G}}(\boldsymbol{r}, \omega) = \frac{1}{4\pi\eta} \left(\frac{e^{-\alpha r}}{r}\boldsymbol{I} + \alpha^{-2}\boldsymbol{\nabla}\boldsymbol{\nabla}\frac{e^{i\mu r} - e^{-\alpha r}}{r}\right), \tag{3.37}$$

with

$$\alpha = (-i\omega\rho_0/\eta)^{1/2}, \quad \mu = \omega/\tilde{c}, \tag{3.38}$$

and

$$\tilde{c} = c\left[1 - \frac{i\omega}{\rho_0 c^2}\left(\frac{4}{3}\eta + \eta_v\right)\right]^{1/2}. \tag{3.39}$$

For an isolated single spherical particle in a fluid, with a body force constraint $\boldsymbol{f}^R$ to satisfy the condition of particle rigidity, the self-mobilities can be analytically derived[18,20,21] as follows:

$$\hat{\mu}_{11}^{\mathrm{tt}}(\omega) = \mu_0^{\mathrm{t}}\frac{9}{2x^2}\frac{2x^2(1 - iy) - (1 + x)y^2 - x^2 y^2}{(1 + x)(9 - 9iy - 2y^2) + x^2(1 - iy)}, \tag{3.40}$$

$$\hat{\mu}_{11}^{\mathrm{rr}}(\omega) = \mu_0^{\mathrm{r}}\frac{3(1 + x)}{3 + 3x + x^2}, \tag{3.41}$$

where $x = \alpha a$, $y = \mu a$, $\mu_0^{\mathrm{t}} = (6\pi\eta a)^{-1}$, and $\mu_0^{\mathrm{r}} = (8\pi\eta a^3)^{-1}$. When the speed of sound is assumed to be infinite, or $\mu = 0$, the solution for an incompressible fluid is obtained. The translation-rotation coupling does not appear in the self-mobility as $\hat{\mu}_{11}^{\mathrm{rt}} = 0$.

To calculate the cross-mobilities, we introduce the Oseen approximation in which the particles are regarded as points. In the Oseen approximation, a particle exerts a Stokeslet (point force); therefore, according to Eq. (3.36), the translation-translation cross-mobility is the Green's function itself:

$$\hat{\boldsymbol{\mu}}_{12}^{\mathrm{tt}}(\boldsymbol{R},\omega) = \hat{\boldsymbol{G}}(\boldsymbol{R},\omega). \tag{3.42}$$

The components of the parallel and perpendicular directions are explicitly given by

$$\hat{\mu}_{12}^{\mathrm{tt}\parallel}(R,\omega) = \mu_0^{\mathrm{t}}\frac{3a}{2\alpha^2 R^3}[(2 - 2i\mu R - \mu^2 R^2)e^{i\mu R} - (2 + 2\alpha R)e^{-\alpha R}], \tag{3.43a}$$

$$\hat{\mu}_{12}^{\mathrm{tt}\perp}(R,\omega) = \mu_0^{\mathrm{t}}\frac{3a}{2\alpha^2 R^3}[(-1 + i\mu R)e^{i\mu R} + (1 + \alpha R + \alpha^2 R^2)e^{-\alpha R}]. \tag{3.43b}$$

The Stokeslet also generates a rotational motion with an angular velocity of $(1/2)\boldsymbol{\nabla}\times\hat{\boldsymbol{v}}_\omega$; therefore, the translation-rotation cross-mobility is given by

$$\hat{\boldsymbol{\mu}}_{12}^{\mathrm{rt}}(\boldsymbol{R},\omega) = -\frac{1}{2}\boldsymbol{\nabla}\times\hat{\boldsymbol{G}}(\boldsymbol{R},\omega), \tag{3.44}$$

which has a perpendicular component only:

$$\hat{\mu}_{12}^{\mathrm{rt}\perp}(R,\omega) = \mu_0^{\mathrm{r}}\frac{a^3}{R^2}(1 + \alpha R)e^{-\alpha R}. \tag{3.45}$$

There are no effects from the fluid compressibility. This result is also derived by considering the velocity field generated by a rotlet (point torque).[22] The rotation-rotation cross-mobility is obtained from the angular velocity generated by a rotlet:

$$\hat{\boldsymbol{\mu}}_{12}^{\mathrm{rr}}(\boldsymbol{R},\omega) = \frac{1}{4}\boldsymbol{\nabla}\times\boldsymbol{\nabla}\times\hat{\boldsymbol{G}}(\boldsymbol{R},\omega). \tag{3.46}$$

Then, each component is given by

$$\hat{\mu}_{12}^{\mathrm{rr}\parallel}(R,\omega) = \mu_0^{\mathrm{r}}\frac{a^3}{R^3}(1 + \alpha R)e^{-\alpha R}, \tag{3.47a}$$

$$\hat{\mu}_{12}^{\mathrm{rr}\perp}(R,\omega) = -\mu_0^{\mathrm{r}}\frac{a^3}{2R^3}(1 + \alpha R + \alpha^2 R^2)e^{-\alpha R}. \tag{3.47b}$$

Using the analytical solutions for an isolated single particle for the self-mobilities and the Oseen approximation for the cross-mobilities, the velocity cross-relaxation functions can be approximated by Eq. (3.12).

References

1 W. van Saarloos and P. Mazur, Physica A **120**, 77 (1983).

2 H. J. H. Clercx and P. P. J. M. Schram, Physica A **174**, 325 (1991).

3 S. Henderson, S. Mitchell, and P. Bartlett, Phys. Rev. Lett. **88**, 088302 (2002).

4 M. Atakhorrami, G. H. Koenderink, C. F. Schmidt, and F. C. MacKintosh, Phys. Rev. Lett. **95**, 208302 (2005).

5 S. Martin, M. Reichert, H. Stark, and T. Gisler, Phys. Rev. Lett. **97**, 248301 (2006).

6 Y. von Hansen, A. Mehlich, B. Pelz, M. Rief, and R. R. Netz, Rev. Sci. Instrum. **83**, 095116 (2012).

7 P. Español, M. A. Rubio, and I. Zúñiga, Phys. Rev. E **51**, 803 (1995).

8 P. Español, Physica A **214**, 185 (1995).

9 Y. Nakayama and R. Yamamoto, Phys. Rev. E **71**, 036707 (2005).

10 Y. Nakayama, K. Kim, and R. Yamamoto, Eur. Phys. J. E **26**, 361 (2008).

11 R. Tatsumi and R. Yamamoto, Phys. Rev. E **85**, 066704 (2012).

12 J. Happel and H. Brenner, *Low Reynolds Number Hydrodynamics*, (Kluwer Academic, Boston, 1983).

13 D. J. Jeffrey and Y. Onishi, J. Fluid Mech. **139**, 261 (1984).

14 M. Reichert and H. Stark, Phys. Rev. E **69**, 031407 (2004).

15 J. D. Jackson, *Classical Electrodynamics* 3rd ed., (Wiley, New York, 1999).

16 B. U. Felderhof, Phys. Fluids **19**, 073102 (2007).

17 B. Cichocki and B. U. Felderhof, Phys. Rev. E **62**, 5383 (2000).

18 D. Bedeaux and P. Mazur, Physica **78**, 505 (1974).

19 B. U. Felderhof, Physica A **389**, 5602 (2010).

20 B. U. Felderhof, Phys. Fluids **19**, 126101 (2007).

21 B. U. Felderhof, Physica A **84**, 569 (1976).

22 S. Kim and S. J. Karrila, *Microhydrodynamics*, (Butterworth-Heinemann, Boston, 1991).

Chapter 4

Velocity relaxation of a particle in a confined compressible fluid

4.1 Introduction

The dynamics of particles dispersed in a fluid flowing through a microchannel are important for many chemical engineering processes, such as membrane separation and microfluidics. The dynamics of fluids and dispersed particles are significantly affected by bounding walls; thus, the transport properties of dispersions in some simple bounding geometries have been studied using analytical methods.[1] While such studies were limited to a steady flow system, recently, the unsteady dynamics of a dispersed particle in a confined fluid have been investigated.[2–8]

In a dispersion system, the momentum of a particle is propagated in the ambient fluid via two mechanisms: viscous diffusion and sound propagation. Each of these mechanisms is accompanied by fluid flow of different character, which affects the particle motion. Here, we consider the velocity relaxation of a particle after adding an impulsive force. In a bulk fluid, part of the particle momentum is transported by a sound wave to an infinite distance in time, and finally, the particle motion is governed by shear flow accompanied by viscous diffusion, which results in the algebraic decay obeying $t^{-3/2}$.[9,10] However, in a fluid confined by walls with stick boundary conditions, both the viscous diffusion and sound propagation are affected by the walls. The viscous diffusion is hampered at the walls, and the accompanying shear flow gradually diminishes; however, the sound wave is repeatedly reflected at the walls and spreads diffusely.[3,4] Consequently, the particle motion is finally governed by flow accompanied by the spreading sound wave. Especially in a fluid confined between two parallel plane walls, the particle velocity relaxation presents a negative t^{-2} long-time decay differently than that presented in a bulk fluid, which is derived by the mode-coupling theory[3] and Green's function method.[4]

In the present study, we investigate the dynamics of a single spherical particle in a fluid confined by two parallel plane walls with stick boundary conditions using a direct numerical simulation approach. We use the smoothed profile method (SPM),[11,12] which is applicable to a compressible fluid.[13] In SPM, rigid fixed wall boundaries can be imposed similar to the representation of rigid

particles.[14] The accuracy of SPM for the present system is confirmed by calculating the steady-state mobility of the particle, which is compared with the approximate analytical solutions. We examine the velocity relaxation of the particle after adding an impulsive force in the direction parallel to the walls. The velocity relaxation function corresponds to the velocity autocorrelation function in a fluctuating system. We first consider an incompressible fluid to investigate the wall effects on the dynamics governed only by viscous diffusion. We then consider a compressible fluid and investigate the particle motion affected by the spreading sound wave arising from reflections at the walls.

4.2   Model

We consider a system in which a single particle is dispersed in a Newtonian fluid confined by two parallel plane walls, as described in Fig. 4.1. The stick boundary conditions are imposed on the walls. The motion of the particle is governed by Newton's and Euler's equations of motion as

$$M\frac{\mathrm{d}}{\mathrm{d}t}\boldsymbol{V} = \boldsymbol{F}^H + \boldsymbol{F}^W + \boldsymbol{F}^E, \quad \frac{\mathrm{d}}{\mathrm{d}t}\boldsymbol{R} = \boldsymbol{V}, \tag{4.1}$$

$$\boldsymbol{I}_p \cdot \frac{\mathrm{d}}{\mathrm{d}t}\boldsymbol{\Omega} = \boldsymbol{N}^H + \boldsymbol{N}^E, \tag{4.2}$$

where $\boldsymbol{R}$, $\boldsymbol{V}$, and $\boldsymbol{\Omega}$ are the position, translational velocity, and rotational velocity of the particle, respectively. The particle has a mass M and a moment of inertia $\boldsymbol{I}_p$. A hydrodynamic force $\boldsymbol{F}^H$ and a torque $\boldsymbol{N}^H$ are exerted on the particle by the fluid, and a repulsive force $\boldsymbol{F}^W$ prevents the particle from overlapping with the walls. A force $\boldsymbol{F}^E$ and a torque $\boldsymbol{N}^E$ are externally applied. The hydrodynamic force and torque are evaluated by simultaneously considering the fluid motion.

The dynamics of fluid are governed by the following hydrodynamic equations:

$$\frac{\partial \rho}{\partial t} + \boldsymbol{\nabla} \cdot (\rho \boldsymbol{v}) = 0, \tag{4.3}$$

$$\frac{\partial \rho \boldsymbol{v}}{\partial t} + \boldsymbol{\nabla} \cdot (\rho \boldsymbol{v} \boldsymbol{v}) = \boldsymbol{\nabla} \cdot \boldsymbol{\sigma} + \rho \phi_P \boldsymbol{f}_P + \rho \phi_W \boldsymbol{f}_W, \tag{4.4}$$

where $\rho(\boldsymbol{r}, t)$ and $\boldsymbol{v}(\boldsymbol{r}, t)$ are the mass density and velocity fields of the fluid, respectively. The stress tensor is given by

$$\boldsymbol{\sigma} = -p\boldsymbol{I} + \eta[\boldsymbol{\nabla}\boldsymbol{v} + (\boldsymbol{\nabla}\boldsymbol{v})^T] + \left(\eta_v - \frac{2}{3}\eta\right)(\boldsymbol{\nabla} \cdot \boldsymbol{v})\boldsymbol{I}, \tag{4.5}$$

50

where $p(\mathbf{r}, t)$ is the pressure, η is the shear viscosity, and η_v is the bulk viscosity. The body force $\rho\phi_P \mathbf{f}_P$ is added such that the rigidity of the particles is satisfied. The external force field $\rho\phi_W \mathbf{f}_W$ is also introduced to impose the stick boundary conditions by two parallel plane walls such that the force $\rho\phi_W \mathbf{f}_W$ constrains the velocity field in the wall region to be zero. Additionally, we assume a barotropic fluid described by $p = p(\rho)$, with the constant speed of sound c being

$$\frac{\mathrm{d}p}{\mathrm{d}\rho} = c^2. \tag{4.6}$$

Equations (4.3)-(4.6) are closed for the variables ρ, $\mathbf{v}$, and p without consideration of energy conservation.

We use the SPM for the direct numerical simulations in the present study. The system is composed of three regions: the fluid, particle, and wall. In SPM, the boundaries between the fluid region and the other regions are expressed by the continuous phase profile function. There are no boundaries between the particle and wall regions because the particle does not penetrate into the wall. For this purpose, we introduce a smoothed profile function $\phi_X(\mathbf{r}, t) \in [0, 1]$, where the index X signifies the region of the particle P or wall W. The function ϕ_X represents the boundary between the regions of the fluid and X, such that $\phi_X = 1$ in region X and $\phi_X = 0$ in the other regions. Using the smoothed profile function, the regions of the fluid and X are smoothly connected through a thin interfacial region with thickness ξ. The detailed mathematical expression of ϕ_X is given in a previous paper.[11]

4.3 Numerical Results

Numerical simulations are performed for a three-dimensional box with periodic boundary conditions. The space is divided into meshes of length Δ, which is a unit length. The units of the other physical quantities are defined by combining $\eta = 1$ and $\rho_0 = 1$ with Δ, where ρ_0 is the fluid mass density at equilibrium. The other parameters are set to $a = 4$, $\xi = 2$, $\rho_p = 1$, $\eta_v = 0$, and $h = 0.05$, where ρ_p is the particle mass density, and h is the time increment of a single simulation step. The geometry of the present system is described in Fig. 4.1. The particle is set on the midway between two walls as $l = H/2$. The ratio of the wall spacing to the particle radius, $H^* = H/a$, is set to various values. The system size is $L_x \times L_y \times L_z = 512 \times 512 \times 32$ for $H^* < 8$ and $L_z = 64$ for $H^* \geq 8$.

We investigate the relaxation of the particle velocity after exerting an impulsive force at the
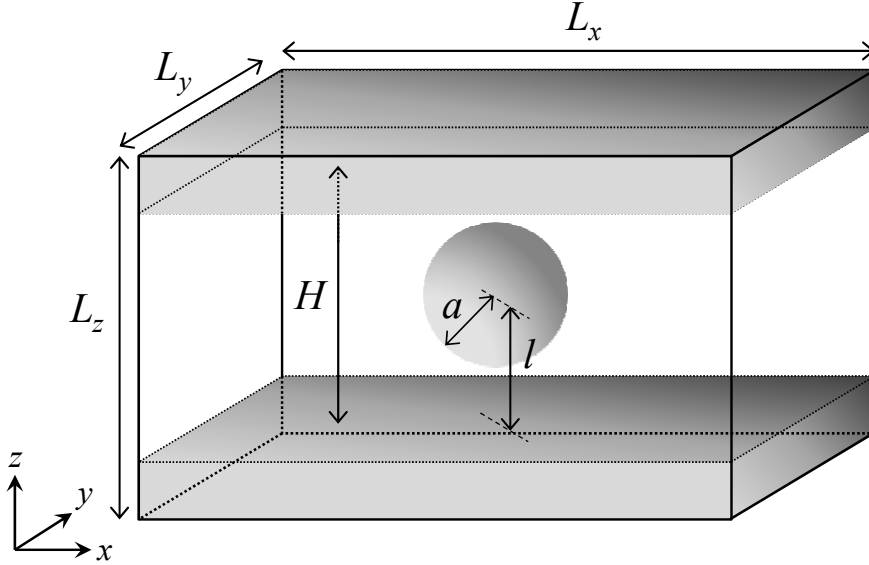
Figure 4.1: Geometry of the present model system. A single spherical particle is in a fluid confined by two parallel plane walls. The particle radius is a, and the wall spacing is H. The particle is located at a height l from the lower wall. The system is considered to be in a simulation box of size $L_x \times L_y \times L_z$. The periodic boundary conditions are imposed on the end of the box in all directions. The walls are set on the top and bottom of the box in the z direction with thickness $(L_z - H)/2$. The walls generate anisotropy for two directions: parallel and perpendicular to the walls. In this figure, the x and y directions are the degenerate parallel directions, and the z direction is the perpendicular direction.

center of the particle. The impulsive force is assumed to be sufficiently small such that the Reynolds and Mach numbers of the flow are sufficiently low. We set the impulsive force to produce an initial particle Reynolds number of $\mathrm{Re}_p = 10^{-3}$. In the considered system, two directions are specified: parallel and perpendicular to the walls; therefore, assuming a low Reynolds number flow, the relaxation of the particle velocity is described as

$$\boldsymbol{V}(t) = \frac{\boldsymbol{P}}{M} \cdot \boldsymbol{\gamma}(t), \tag{4.7}$$

$$\boldsymbol{\gamma}(t) = \gamma^{\|}(t)(\boldsymbol{I} - \hat{\boldsymbol{z}}\hat{\boldsymbol{z}}) + \gamma^{\perp}(t)\hat{\boldsymbol{z}}\hat{\boldsymbol{z}}, \tag{4.8}$$

where $\boldsymbol{P}$ is the impulsive force exerted on the particle at $t = 0$ and $\hat{\boldsymbol{z}}$ is the unit vector in the z direction. The velocity relaxation tensor $\boldsymbol{\gamma}(t)$ also depends on the wall spacing H and the distance of the particle from the lower wall l. In the present study, we focus on the parallel motion of the particle $\gamma^{\|}(t)$; therefore, in the following section, we represent the velocity relaxation function in the parallel direction by $\gamma(t)$ for simplicity. For this reason, collisions of the particle against the wall will not occur, and the direct interactions between a particle and wall, including the overlap repulsion force,
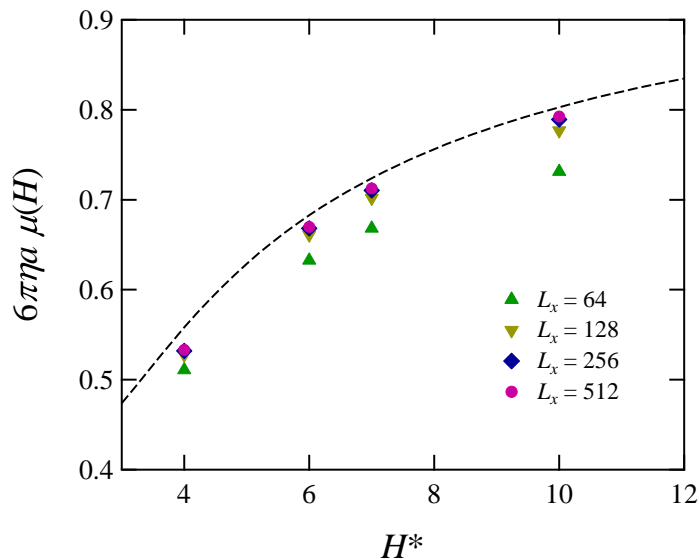
Figure 4.2: Wall spacing dependence of the mobility of a single particle in a fluid confined by two parallel plane walls. The length of the simulation box sides parallel to the walls are changed to $L_x = L_y = 64, 128, 256,$ and 512 to investigate the effect of the periodic boundary condition. The broken line represents the analytical solution given by Eq. (4.11).

are not considered in the present simulations. According to the fluctuation-dissipation theorem, the velocity relaxation function is equivalent to the velocity autocorrelation function in a fluctuation system:

$$\boldsymbol{\gamma}(t) = \frac{M}{k_B T} \langle \boldsymbol{V}(0)\boldsymbol{V}(t) \rangle, \tag{4.9}$$

where k_B is the Boltzmann constant, and T is the thermodynamic temperature.

The important time scales in the dynamics of a single particle are those of viscous diffusion and sound propagation over the length of the particle radius: $\tau_\nu = a^2/\nu$ and $\tau_c = a/c$, respectively, where $\nu = \eta/\rho_0$ is the kinematic viscosity. We define the compressibility factor by the ratio of these time scales as

$$\varepsilon = \frac{\tau_c}{\tau_\nu} = \frac{\nu}{ac}, \tag{4.10}$$

which provides a measure of the importance of sound propagation in the dynamics of a single particle. In the present simulations, we adjust the fluid compressibility by the compressibility factor.

4.3.A Steady-state mobility in an incompressible fluid

First, we estimate the particle mobility μ in steady state for accuracy testing. In these simulations, a constant force was continuously exerted on the particle in the direction parallel to the walls. The mobility was calculated as the ratio of the particle velocity to the added force after reaching steady state. The mobilities in such situations have been studied by Faxén using analytical theories.[1,15] The solution was given as the power series of the ratio of the wall spacing to particle radius, in which the first few terms were derived as

$$6\pi\eta a\mu(H) = 1 - 1.004\lambda + 0.418\lambda^3$$

$$+0.21\lambda^4 - 0.169\lambda^5 + O(\lambda^6), \tag{4.11}$$

where $\lambda = 2/H^*$. The simulation results are presented in Fig. 4.2 and are compared with the approximate solutions given by Eq. (4.11). The simulations were performed with the various system side lengths in parallel directions to the walls, L_x and L_y ($L_x = L_y$), to investigate the system size effects due to the periodic boundary condition, which are diminished to an insignificant level at $L_x \geq 256$. However, the simulation results underestimate the mobility even at $L_x = 512$; the deviations from the solutions given by Eq. (4.11) are less than 2% for $H^* \geq 6$ and approximately 5% only for $H^* = 4$. As for $H^* = 4$, however, because the order of the power λ^6 is still 1, a truncation error of a few percent arises in Eq. (4.11). Therefore, the simulation error for $H^* = 4$ can be less than 5%.

From the present results, the walls with stick boundary conditions are successfully implemented by SPM. The implementation of confinement by different geometries is also available in SPM.

4.3.B Velocity relaxation in an incompressible fluid

Here, we consider an incompressible fluid as a solvent fluid. To treat an incompressible fluid, we assume an infinite speed of sound in Eq. (4.6) and ignore the deviation of the fluid density. With this assumption and the mass conservation law Eq. (4.3), the solenoidal condition for the velocity field is derived as

$$\nabla \cdot \boldsymbol{v} = 0. \tag{4.12}$$

Therefore, Eqs. (4.4), (4.5), and (4.12) were solved in combination as the hydrodynamic equations.

The simulation results of the velocity relaxation functions for wall spacings $H^* = 4$ and 6 are presented in Fig. 4.3. The relaxation functions decrease monotonically, and the reduction rate
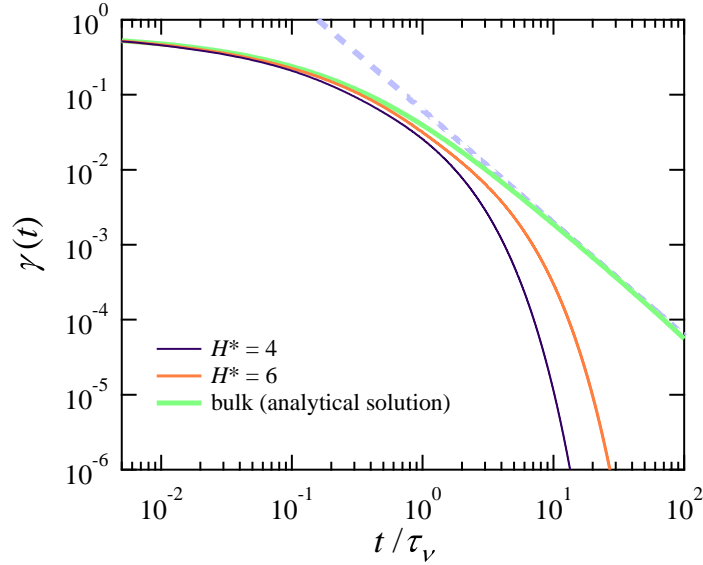
Figure 4.3: Velocity relaxation functions of a particle in an incompressible fluid confined by two parallel plane walls. The wall spacings are $H^* = 4$ and 6. The analytical solution of the corresponding function in a bulk fluid is also presented.[16] The bold dotted line represents the long-time tail $At^{-3/2}$, as given by Eq. (4.13).

increases with a decrease in the wall spacing H^*. Exponential long-time decay is observed, as derived from the analytical theories.[17] Such decay contrasts the relaxation function in a bulk fluid, which describes long-time decay obeying the power law given by[10]

$$\gamma^{\text{bulk}}(t) = \frac{1}{9\sqrt{\pi}} \frac{\rho_p}{\rho_0} \left(\frac{\tau_\nu}{t} \right)^{3/2} \quad \text{as} \ \ t \to \infty. \tag{4.13}$$

The exponential decay of the relaxation function is expected to reflect the loss of fluid momentum at the walls with stick boundary conditions. Therefore, the time when the relaxation function in a confined fluid starts to remarkably fall below that in a bulk fluid is related to the time scale when the fluid flow generated by the particle reaches the walls. In an incompressible fluid, the temporal evolution of the fluid flow is only accompanied by viscous diffusion, whose time scale over the distance between the particle surface and the wall $(H/2 - a)$ is given by $\tau_\nu^\dagger = (H/2 - a)^2/\nu = (H^*/2 - 1)^2\tau_\nu$. For the wall spacings $H^* = 4$ and 6, the viscous diffusion time scales are $\tau_\nu^\dagger/\tau_\nu = 1$ and 4, respectively. As demonstrated in Fig. 4.3, the starting time of the deviation of the function from that in a bulk fluid corresponds to the time scales $\tau_\nu^\dagger$.

The velocity fields around the particle with various wall spacings at the time $t/\tau_\nu = 2.81$ are displayed in Fig. 4.4. Compared with a bulk fluid, the attenuation of fluid velocity is clearly observed in a confined fluid with $H^* = 4$, corresponding to the decay of the shear flow or the
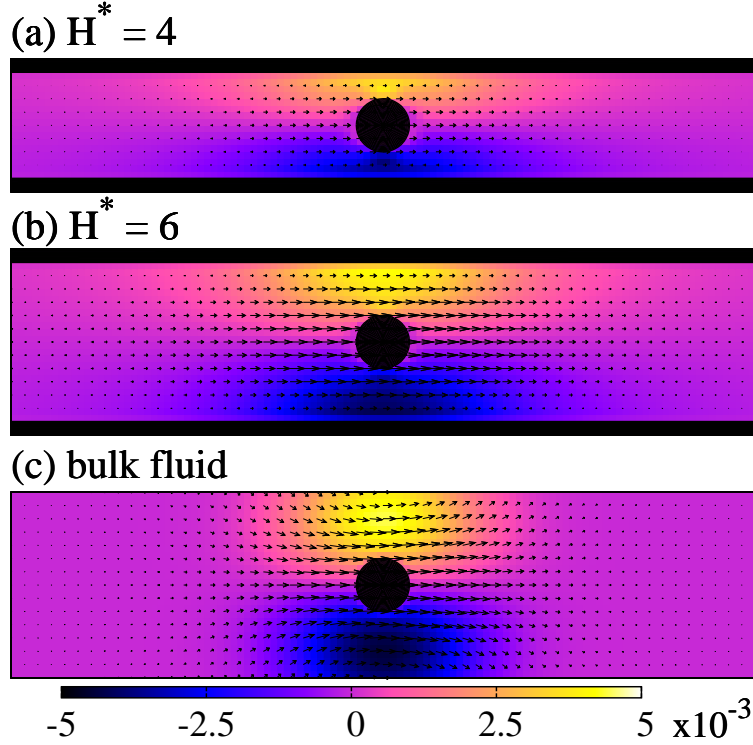
Figure 4.4: Velocity fields around the particle at $t/\tau_\nu = 2.81$ in confined fluids with a wall spacing of (a) $H^* = 4$ and (b) $H^* = 6$ and (c) in a bulk fluid are shown. The walls are set on the upper and lower boundaries of the images for the confined fluids, and the corresponding region is presented for the bulk fluid. The cross-sections presented here are perpendicular to the walls and parallel to the impulsive force direction and include the particle center. The direction of the impulsive force is to the right in the images, and the particle is represented by a black circle. The vorticity of the velocity field $\nabla \times \boldsymbol{v}$ is described using a color scale, moving from negative (darker) to positive (lighter) vorticity. The vorticity is normalized by the factor of τ_ν/Re_p.

vorticity by the walls. However, the attenuation of fluid velocity is not observed for $H^* = 6$. This result coincides with the fact that the time $t/\tau_\nu = 2.81$ is earlier than the viscous diffusion time scale for $H^* = 6$, namely, $\tau_\nu^\dagger/\tau_\nu = 4$. The walls restrict the viscous diffusion of the flow field to form a laminar flow, which corresponds to the extended distribution of the vorticity along the walls.

4.3.C Velocity relaxation in a compressible fluid

In a compressible fluid, the velocity relaxation function exhibits essentially different behaviors from those in an incompressible fluid. The simulation results of the relaxation functions are presented in Fig. 4.5. Remarkable differences are the sign inversion and the subsequent negative long-time algebraic decay. The power of the long-time decay is t^{-2}, and the coefficient is analytically derived as[3,4]

$$\gamma(t) = -\frac{3}{8}\frac{\rho_p}{\rho_0}\frac{\varepsilon^2}{H^*}\left(\frac{\tau_\nu}{t}\right)^2 \quad \text{as } t \to \infty. \tag{4.14}$$
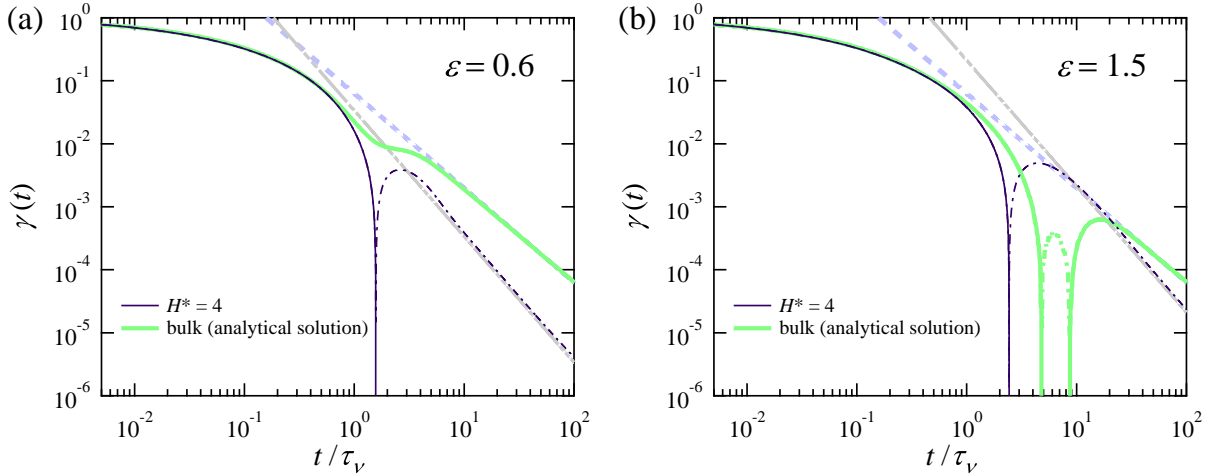
Figure 4.5: Velocity relaxation functions of a particle in a compressible fluid confined by two parallel plane walls with the wall spacing $H^* = 4$. The compressibility factors are (a) $\varepsilon = 0.6$ and (b) $\varepsilon = 1.5$. The analytical solutions of the corresponding functions in a bulk fluid are also presented.[18,19] The functions are described by solid lines (positive values) and dashed-dotted lines (negative values). The bold dotted lines represent the positive long-time tail $At^{-3/2}$, given by Eq. (4.13). The bold dashed-two dotted lines represent the negative long-time tail $-Bt^{-2}$, given by Eq. (4.14).

In the present simulation results, the asymptotic approaches to Eq. (4.14) are accurately reproduced. In a bulk fluid, the long-time decay is positive and proportional to $t^{-3/2}$, given by Eq. (4.13) as an incompressible fluid. Although the sign inversion can occur for a large compressibility factor as $\varepsilon = 1.5$, the relaxation function eventually becomes positive.

For the compressibility factor $\varepsilon = 0.6$, the temporal evolution of the velocity field in a confined fluid is compared with that in a bulk fluid in Fig. 4.6. The flow accompanied by a sound wave is source-sink flow: the flow moves from the source (positive divergence region) to the sink (negative divergence region). The divergence of the velocity field corresponds to the fluid density deviation as

$$\boldsymbol{\nabla} \cdot \boldsymbol{v} = -\frac{D}{Dt} \ln \frac{\rho}{\rho_0}. \tag{4.15}$$

In a bulk fluid, a sound wave propagates away from the particle; therefore, eventually, the effect of the sound wave on the particle motion disappears, and the particle motion is governed by shear flow accompanied by viscous diffusion. However, in a confined fluid, a sound wave is repeatedly reflected at the walls and continuously affects the particle motion. Multiple reflections at the walls results in the spreading of sound wave, which is known as the overdamped diffusive mode.[3,4] Because viscous diffusion is prevented by the walls and the corresponding shear flow gradually disappears, the
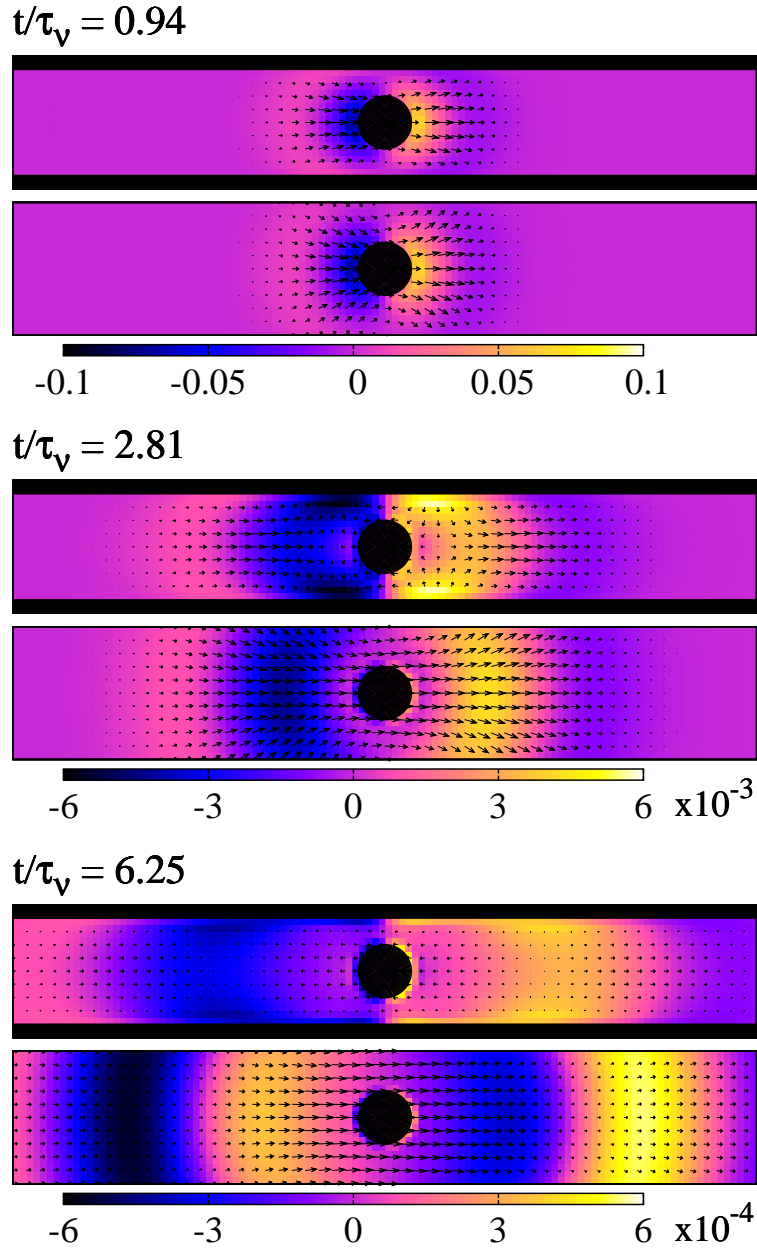
Figure 4.6: Temporal evolution of the velocity fields in a confined fluid with $H^* = 4$ (upside in each time) and in a bulk fluid (downside in each time). The compressibility factor is $\varepsilon = 0.6$. The walls are set on the upper and lower boundaries of the images for the confined fluids, and the corresponding regions are presented for the bulk fluids. The cross-sections presented here are perpendicular to the walls and parallel to the impulsive force direction and include the particle center. The direction of the impulsive force is to the right in the images, and the particle is represented by a black circle. The divergence of the velocity field $\boldsymbol{\nabla} \cdot \boldsymbol{v}$ is described using a color scale, moving from negative (darker) to positive (lighter) vorticity. The divergence is normalized by the factor of τ_ν/Re_p.
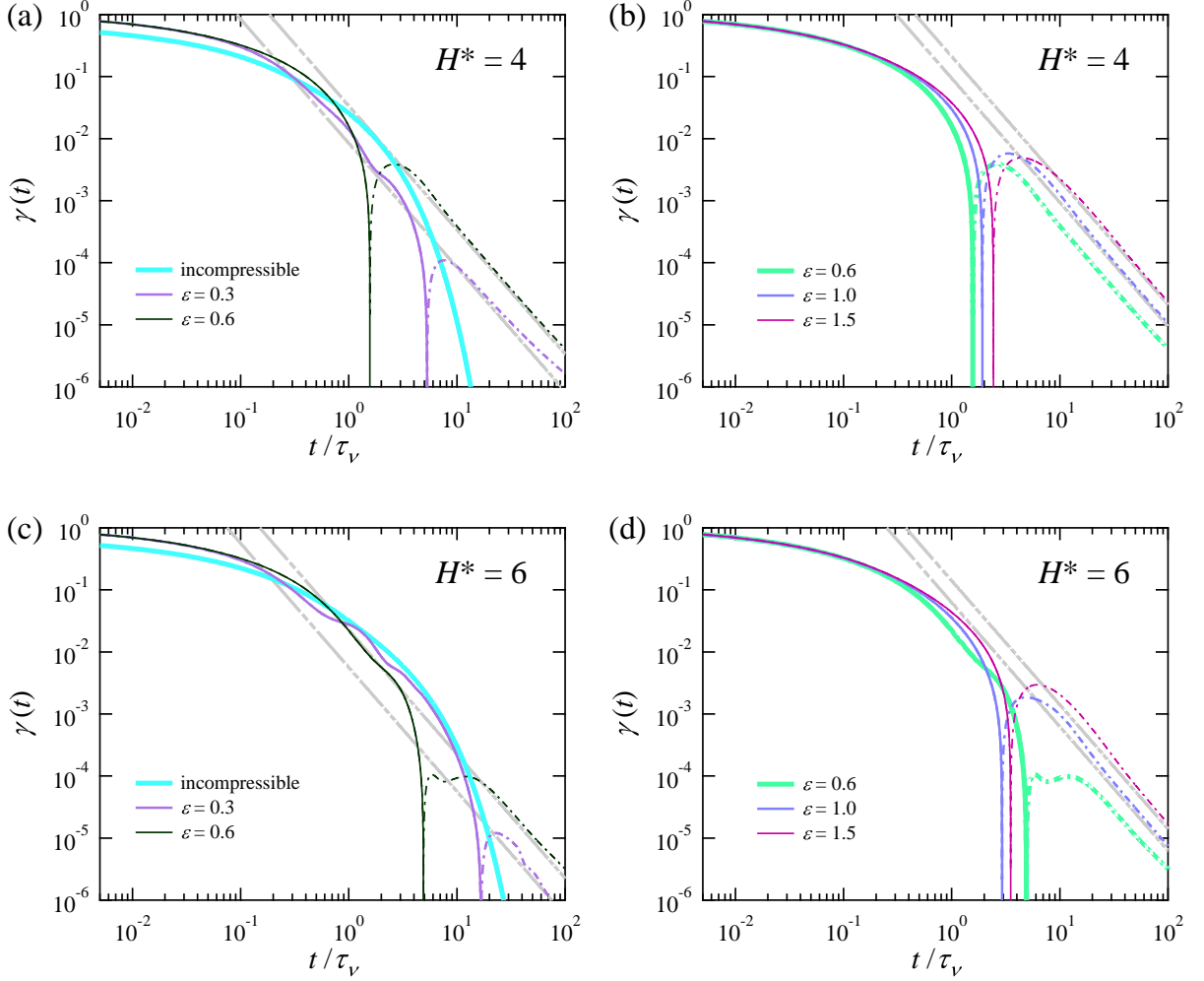
Figure 4.7: Velocity relaxation function of a particle in a compressible fluid confined between two flat walls. The wall spacings are (a, b) $H^* = 4$ and (c, d) $H^* = 6$. The compressibility factor has values of $\varepsilon = 0.3$, 0.6, 1.0, and 1.5. The simulation results are represented by solid lines (positive values) and dashed-dotted lines (negative values). The bold dashed-two dotted lines represent the negative long-time tail $-Bt^{-2}$, as given by Eq. (4.14).

particle motion is eventually governed by the sound wave. The spreading sound wave is associated with backward fluid flow and causes backtracking of the particle, which corresponds to the negative velocity relaxation function.

The long-time decay of the particle velocity reflects the eventual mechanism transmitting the fluid flow: viscous diffusion or sound propagation. In a bulk fluid, the particle velocity finally decays, obeying Eq. (4.13), which corresponds to viscous diffusion of the shear flow. The volume of the viscous diffusion region at time t is proportional to $(\nu t)^{3/2}$. In a confined fluid, the different long-time decay Eq. (4.14) appears. This negative decay originates from the spreading sound wave, whose spreading volume at time t is proportional to $H(ct)^2$.
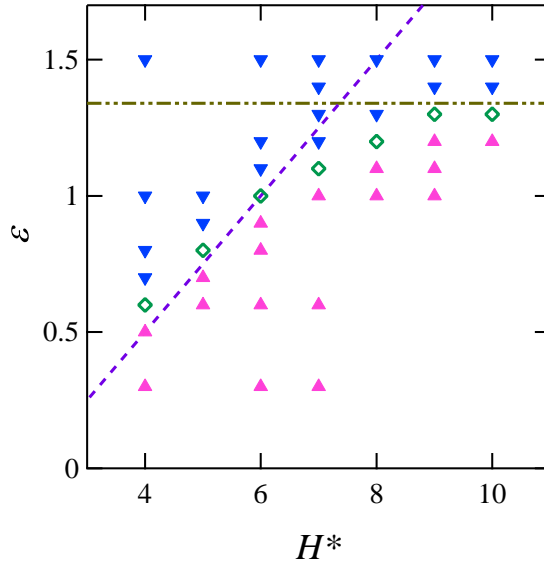
Figure 4.8: Classification of calculated velocity relaxation functions for various wall spacings and compressibility factors. The time when the sign inversion of the velocity relaxation function occurs non-monotonically changes with respect to the compressibility factor. For each wall spacing, with the increase in the compressibility factor, the decrease and increase of the time of the sign inversion are represented by upward and downward triangles, respectively. The time of the sign inversion is minimized at the characteristic compressibility factor, which is represented by open diamond. The broken line represents Eq. (4.16) with $\varepsilon^{\dagger} = 1$. The dashed double-dotted line represents $\varepsilon = 1.34$.

In Fig. 4.7, the relaxation functions with wall spacings $H^* = 4$ and 6 for various compressibility factors are displayed. Discrepancies of long-time decay with Eq. (4.14) for small compressibility factors are presumed to result from system size effects due to the periodic boundary conditions, which will appear after the time when the sound wave generated by the particle reaches the end of the system: $t = (L_x/2 - a)/c = (L_x/2a - 1)\varepsilon\tau_\nu$. The time when the sign inversion occurs changes non-monotonically with respect to the fluid compressibility. With an increase in the compressibility factor, the time of the sign inversion occurs earlier when the compressibility factor is small; however, the sign inversion occurs later when the compressibility factor is large. In other words, there is a compressibility factor at which the time of the sign inversion is minimized, which we call the characteristic compressibility factor. The characteristic compressibility factor depends on the wall spacing H^*; for example, from Fig. 4.7, the characteristic compressibility factors are presumed to be $\varepsilon \approx 0.6$ for $H^* = 4$ and $\varepsilon \approx 1.0$ for $H^* = 6$. More detailed evaluations of the characteristic compressibility factors for various wall spacings are provided in Fig. 4.8.

The sign inversion of the velocity relaxation function, namely, the backtracking of the particle, is expected to occur after the sound wave reflected at the wall reaches the particle. The time scale
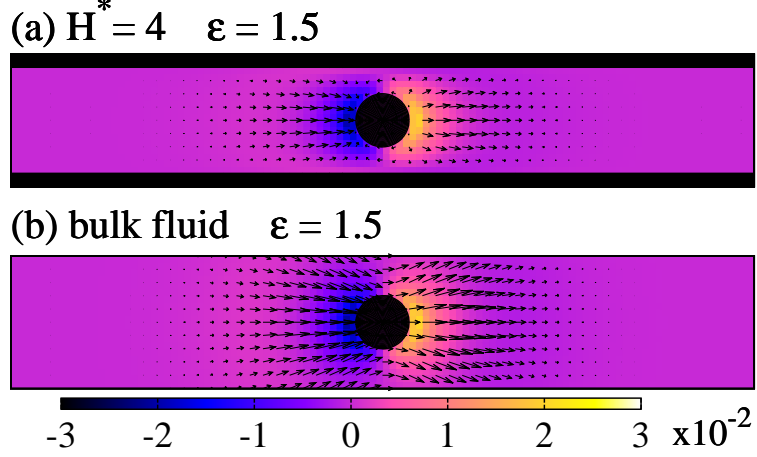
60

Figure 4.9: Velocity fields around the particle at $t/\tau_\nu = 2.81$ (a) in a confined fluid with wall spacing $H^* = 4$ and (b) in a bulk fluid. The compressibility factor is $\varepsilon = 1.5$. The walls are set on the upper and lower boundaries of picture for the confined fluid, and the corresponding region is exhibited for the bulk fluid. The cross-sections shown here are perpendicular to the walls and parallel to the impulsive force direction with including the particle center. The direction of the impulsive force is to the right in the pictures and the particle is represented by a black circle. The divergence of the velocity field $\nabla \cdot \boldsymbol{v}$ is described by a color scale, going from negative (darker) to positive (lighter) vorticity. The divergence is normalized by the factor of τ_ν/Re_p.

of this event is estimated by $\tau_c^\dagger = 2(H/2 - a)/c = (H^* - 2)\varepsilon\tau_\nu$. Moreover, sufficient decay of the shear flow around the particle is required, and the time scale of the shear flow decay is $\tau_\nu^\dagger$, as given in the previous section. Here, we define the confined compressibility factor as the ratio of the two time scales:

$$\varepsilon^\dagger = \frac{\tau_c^\dagger}{\tau_\nu^\dagger} = \frac{4\varepsilon}{H^* - 2}. \tag{4.16}$$

When the confined compressibility factor is small, $\varepsilon^\dagger < 1$, the spreading of the sound wave caused by reflection at the walls progresses faster than the decay of the shear flow. For smaller confined compressibility factors, the sound wave spreads and is weakened more rapidly; therefore, further reduction of the shear flow is required to cause backtracking of the particle. In short, when $\varepsilon^\dagger < 1$ is satisfied, backtracking of the particle occurs at a later time for a smaller confined compressibility factor. However, when the confined compressibility factor is large, $\varepsilon^\dagger > 1$, the reflected sound wave reaches the particle after sufficient decay of the shear flow; therefore, particle backtracking occurs at a later time for a larger confined compressibility factor. Consequently, the characteristic compressibility factor is expected to satisfy $\varepsilon^\dagger \approx 1$. In Fig. 4.8, the line of Eq. (4.16) with $\varepsilon^\dagger = 1$ almost coincides with the characteristic compressibility factors at $H^* \leq 6$; however, this relation fails at $H^* > 6$, where another mechanism of backtracking must be considered.

For the compressibility factor $\varepsilon = 1.5$, a comparison of the velocity fields in confined and bulk fluids at time $t/\tau_\nu = 2.81$ is presented in Fig. 4.9. Although this time is earlier than the time $\tau_c^\dagger$, the relaxation function in the confined fluid is negative, as illustrated in Fig. 4.5(b); therefore, the backtracking is caused by the pressure from the sound wave remaining in the vicinity of the particle. Backtracking by this mechanism is also observed in a bulk fluid when the compressibility factor is sufficiently large,[19, 20] and the condition for which the backtracking occurs is estimated as $\varepsilon \geq 1.34$ from the analytical solution.[18, 19] There is only a slight difference in the divergence of the velocity field between the confined and bulk fluids; however, in a confined fluid, because shear flow is diminished by the walls, backtracking by a sound wave can occur at an earlier time than in a bulk fluid, as demonstrated in Fig. 4.5(b). Considering this mechanism of particle backtracking, the characteristic compressibility factor will eventually converges to $\varepsilon = 1.34$ with an increase in the wall spacing H^*. The successive change in the dependence of the characteristic compressibility factor on the wall spacing, namely, from $\varepsilon^\dagger = 1$ to $\varepsilon = 1.34$, is observed in Fig. 4.8. The wall spacing at which this crossover occurs is estimated as $H^* \approx 7.4$.

4.4   Conclusion

We investigated the dynamics of a single particle in a fluid confined by two parallel plane walls using SPM to perform direct numerical simulations. In particular, we calculated the velocity relaxation of the particle after an impulsive force was added in the direction parallel to the walls. The velocity relaxation function corresponds to the velocity autocorrelation function in a fluctuating system.

In an incompressible fluid, the relaxation function decayed more rapidly in a confined fluid than in a bulk fluid; the long-time decay was exponential differently from the power law $t^{-3/2}$ observed in a bulk fluid. The rapid decay reflects the loss of shear flow due to the hindrance of viscous diffusion by the walls. Therefore, the time when the relaxation function in a confined fluid falls below that in a bulk fluid corresponds to the time scale of viscous diffusion over the distance between the particle surface and the walls, $\tau_\nu^\dagger$.

In a compressible fluid, sign inversion and subsequent negative long-time decay obeying t^{-2} were observed in the velocity relaxation functions. A corresponding spreading sound wave arising from the multiple reflections at the walls was also observed. The time of the sign inversion changed non-monotonically with respect to the compressibility factor; that is, the time of the sign inversion was minimized at the characteristic compressibility factor. The characteristic compressibility factor

satisfies $\varepsilon^\dagger = 1$ when the wall spacing is small and is given by $\varepsilon = 1.34$ when the wall spacing is large, where the confined compressibility factor $\varepsilon^\dagger$ is defined by Eq. (4.16). The crossover of the dependence of the characteristic compressibility factor on the wall spacing is estimated to be $H^* \approx 7.4$. The backtracking of the particle is caused by the spreading sound wave arising from reflections at the walls when the characteristic compressibility factor satisfies $\varepsilon^\dagger = 1$ and is caused by the remaining sound wave in the vicinity of the particle when the characteristic compressibility factor is given by $\varepsilon = 1.34$. Backtracking via the latter mechanism can also occur in a high compressible bulk fluid.

References

1 J. Happel and H. Brenner, *Low Reynolds Number Hydrodynamics* (Kluwer Academic, Boston, 1983).

2 M. H. J. Hagen, I. Pagonabarraga, C. P. Lowe, and D. Frenkel, Phys. Rev. Lett. **78**, 3785 (1997).

3 I. Pagonabarraga, M. H. J. Hagen, C. P. Lowe, and D. Frenkel, Phys. Rev. E **59**, 4458 (1998).

4 B. U. Felderhof, J. Chem. Phys. **124**, 054111 (2006).

5 D. Frydel and S. A. Rice, Mol. Phys. **104**, 1283 (2006).

6 D. Frydel and S. A. Rice, Phys. Rev. E **76**, 061404 (2007).

7 B. U. Felderhof, J. Fluid Mech. **637**, 285 (2009).

8 B. U. Felderhof, J. Fluid Mech. **644**, 97 (2010).

9 R. Zwanzig and M. Bixon, Phys. Rev. A **2**, 2005 (1970).

10 B. Cichocki and B. U. Felderhof, Phys. Rev. E **62**, 5383 (2000).

11 L. Bocquet and J.-L. Barrat, Europhys. Lett. **31**, 455 (1995); J. Phys.: Condens. Matter **8**, 9297 (1996).

12 Y. Nakayama and R. Yamamoto, Phys. Rev. E **71**, 036707 (2005).

13 Y. Nakayama, K. Kim, and R. Yamamoto, Eur. Phys. J. E **26**, 361 (2008).

14 R. Tatsumi and R. Yamamoto, Phys. Rev. E **85**, 066704 (2012).

15 X. Luo, M. R. Maxey, and G. E. Karniadakis, J. Comput. Phys. **228**, 1750 (2009).

16 H. Faxén, Ann. Phys. **68**, 89 (1922).

17 L. D. Landau and E. M. Lifshitz, *Fluid Mechanics* (Pergamon, London, 1959).

18 D. Bedeaux and P. Mazur, Physica **78**, 505 (1974).

19 B. U. Felderhof, Phys. Fluids **19**, 126101 (2007).

20 B. U. Felderhof, J. Chem. Phys. **123**, 044902 (2005).

Chapter 5

General conclusion

This dissertation is devoted to the study of the influence of the fluid compressibility on the dynamics of particle dispersions. For this purpose, first of all, we constructed the direct numerical simulation method for dispersed particles in a compressible fluid (**Chapter 2**). By using this direct numerical simulation method, we investigated the fluid compressibility effects on the propagation process of hydrodynamic interactions in some simple situations (**Chapter 3** and **4**).

In **Chapter 2**, we constructed the direct numerical simulation method for dispersed particles in a compressible fluid; rather, we extended the SPM to be applicable to dispersions with compressible host fluids. The validity of the method was confirmed by calculating the velocity relaxation function of a single spherical particle in a compressible fluid. The effects of compressibility on the velocity relaxation were also observed. As shown in Fig. 2.1, there are two-stage relaxation in a low-compressibility fluid and backtracking motion in a high-compressibility fluid. These particle motions were interpreted in terms of the fluid density deviation around the particle. The propagation speed of the sound pulse from the particle is governed by the fluid compressibility as shown in Fig. 2.2. In a low-compressibility fluid, the sound pulse immediately propagates and the influence of the sound on the particle motion disappears; by contrast, in a high-compressibility fluid, the sound pulse propagation is quite slow to prolong the influence of the sound. The effects of compressibility on the fluid velocity field were also observed, which was essentially understood to arise from changes in the time evolution of the source-sink flow (doublet flow) component caused by the compressibility (see Figs. 2.3 and 2.4). Additionally, by introducing the random stress on the fluid to the present simulation method, the motion of a single particle in a fluctuating fluid was also reproduced. The calculated velocity autocorrelation function of the particle showed good agreement with the analytical solution of the relaxation function. This result confirms the validity of the fluctuation-dissipation theorem in the present simulation method.

In **Chapter 3**, we investigated the fluid compressibility effects on the propagation process of hydrodynamic interactions between two spherical particles. Hydrodynamic interactions were estimated by the velocity cross-relaxation functions between particles, which are equivalent to the

velocity cross-correlation functions in a fluctuating system. Because the cross-relaxation function reflects the fluid flow field around the particles, first of all, we investigated the flow field by theoretical analysis, which showed that a doublet flow and shear flow are generated accompanied by sound propagation and viscous diffusion, respectively, as implied in **Chapter 2**. The velocity cross-relaxation functions were calculated by direct numerical simulation, and the results were interpreted in relation to the temporal evolution of the flow field. In an incompressible fluid, as shown in Fig. 3.2, the time at which the behavior of the cross-relaxation function changes was related to the time scale of viscous diffusion over the particle separation τ_ν^*, which is only the time scale characterizing the temporal evolution of hydrodynamic interactions in an incompressible fluid. Correspondingly, hydrodynamic interactions were interpreted to propagate instantaneously at the infinite speed of sound, along with subsequent temporal evolution by viscous diffusion. In a compressible fluid, sound propagates between particles in a finite time, which scales as τ_c^*. The effect of the order of magnitude relation between the two time scales τ_ν^* and τ_c^* on the cross-relaxation function was observed; an interactive compressibility factor ε^* was defined as the ratio of the two time scales given by Eq. (3.33). In our simulation results as summarized in Fig. 3.8, the reversal of the order of arrival of sound propagation and viscous diffusion at the other particle was observed at $\varepsilon^* \geq 0.175$. In this case, the hydrodynamic interactions were largely governed by viscous diffusion. In short, when the interactive compressibility factor is sufficiently small, the temporal evolution of hydrodynamic interactions does not qualitatively change from that for an incompressible fluid; however, when the interactive compressibility factor is large, qualitatively different temporal evolution of hydrodynamic interactions can be observed.

In **Chapter 4**, we investigated the fluid compressibility effects on the hydrodynamic interactions between a particle and walls. For this purpose, we examined the dynamics of a single spherical particle in a fluid confined by two parallel plane walls. The walls with the stick boundary conditions were introduced by applying the principle of SPM. We calculated the velocity relaxation function of the particle after an impulsive force is added in the direction parallel to the walls, which corresponds to the velocity autocorrelation function of the particle motion along the walls in a fluctuating system. In an incompressible fluid, as shown in Fig. 4.3, the exponential decay of the relaxation function was observed. This decay is more rapid than that in a bulk fluid obeying the power law $t^{-3/2}$. The rapid decay reflects the loss of shear flow due to the hindrance of viscous diffusion by the walls. The time when the relaxation function in a confined fluid falls below from that in a bulk

fluid was related to the time scale of viscous diffusion over the distance between the particle surface and the walls, $\tau_\nu^\dagger$. In a compressible fluid, as shown in Fig. 4.5, the sign inversion and the negative long-time tail t^{-2} of the relaxation functions were observed. The negative long-time tails observed in the simulation results were coincident with analytical solution given by Eq. (4.14). Sound wave was repeatedly reflected at the walls to spread diffusely as observed in Fig. 4.6 and caused the negative long-time tail decay of the particle motion. The sign inversion of the velocity relaxation function reflects the diminishing shear flow and the onset of backward flow accompanied by sound wave. The time of sign inversion changed non-monotonically with respect to the compressibility factor as observed in Fig. 4.7; in other words, the time of the sign inversion was minimized at the characteristic compressibility factor. As presented in Fig. 4.8, the characteristic compressibility factor satisfies $\varepsilon^\dagger = 1$ when the wall spacing is small and is given by $\varepsilon = 1.34$ when the wall spacing is large, where the confined compressibility factor $\varepsilon^\dagger$ is defined by Eq. (4.16). The crossover of the dependence of the characteristic compressibility factor on the wall spacing is estimated to be $H^* \approx 7.4$. The backtracking of the particle is caused by the spreading sound wave arising from reflections at the walls when the characteristic compressibility factor satisfies $\varepsilon^\dagger = 1$ and is caused by the remaining sound wave in the vicinity of the particle when the characteristic compressibility factor is given by $\varepsilon = 1.34$. Backtracking via the latter mechanism can also occur in a high compressible bulk fluid.

In this dissertation, we clarified the fluid compressibility effects on the dynamics of dispersed particles for some simple situations. Although these results gave us the several aspects of the fluid compressibility effects, they are still not enough to understand every phenomenon associated with the fluid compressibility. As for the particle-particle hydrodynamic interactions, many-body effects will be significant in a concentrated dispersion. In such a case, multiple sound scattering by particles will occur and thereby will prolong the compressibility effects on the dynamics of the dispersed particles.[1] The analysis of such many-body effects in a compressible fluid is required for the ultrasound spectroscopy when the particle size is evaluated from the measured acoustic properties of a dispersion.[2,3] As for the particle-wall hydrodynamic interactions, the geometry of the confinement is also an important factor. The power of the negative long-time tail of the velocity relaxation function is indicated to depend on the number of dimensions which are not geometrically confined;[3] for example, the long-time decay obeys $t^{-3/2}$ when the confining geometry is a circular tube[4,5] differently from the power law t^{-2} in a fluid confined by two parallel plane walls. However,

including the fluid compressibility effects, the dynamics of dispersed particles in various confining geometries is still not clear. Additionally, hydrodynamic interactions between particles in a confined fluid is also an interesting and important problem to understand the dynamics of dispersions in a microchannel.[6,7] By use and development of the direct numerical simulation method constructed in the present studies, the above problems are expected to be solved in the future.

References

1 A. F. Bakker and C. P. Lowe, J. Chem. Phys. **116**, 5867 (2002).

2 A. S. Dukhin and P. J. Goetz, *Ultrasound for Characterizing Colloids: Particle Sizing, Zeta Potential, Rheology* (Elsevier, Amsterdam, 2002).

3 D. J. McClements, Langmuir **12**, 3454 (1996).

4 M. H. J. Hagen, I. Pagonabarraga, C. P. Lowe, and D. Frenkel, Phys. Rev. Lett. **78**, 3785 (1997).

5 B. U. Felderhof, J. Fluid Mech. **644**, 97 (2010).

6 D. Frydel and H. Diamant, Phys. Rev. Lett. **104**, 248302 (2010).

7 B. U. Felderhof, J. Chem. Phys. **134**, 024505 (2011).

Acknowledgements

List of Publications

Chapter 2

R. Tatsumi and R. Yamamoto, "Direct numerical simulation of dispersed particles in a compressible fluid," Phys. Rev. E, **85**, 066704 1-6, (2012).

Chapter 3

R. Tatsumi and R. Yamamoto, "Propagation of hydrodynamic interactions between particles in a compressible fluid," Phys. Fluids, **submitted**.

Chapter 4

R. Tatsumi and R. Yamamoto, "Velocity relaxation of a particle in a confined compressible fluid," J. Chem. Phys., **submitted**.

Not included in the PhD thesis

R. Tatsumi and Y. Yoshimura, "Solvophobic effects on an infinitely-thin hard needle in a three-dimensional square-well fluid," J. Phys. Soc. Jpn., **78**, 074002 1-10, (2009).